LOW-DIMENSIONAL MODELS OF COHERENT STRUCTURES IN TURBULENCE

Philip J. HOLMES[a,b], John L. LUMLEY[c], Gal BERKOOZ[c,d], Jonathan C. MATTINGLY[a], Ralf W. WITTENBERG[a]

[a]*Program in Applied and Computational Mathematics, Princeton University, Princeton, NJ 08544, USA*

[b]*Department of Mechanical and Aerospace Engineering, Princeton University, Princeton, NJ 08544, USA*

[c]*Sibley School of Mechanical and Aerospace Engineering, Cornell University, Ithaca, NY 14853, USA*

[d]*BEAM Technologies, Inc., 110 N. Cayuga St., Ithaca, NY 14850, USA*

ELSEVIER

AMSTERDAM – LAUSANNE – NEW YORK – OXFORD – SHANNON – TOKYO

ELSEVIER

Physics Reports 287 (1997) 337–384

PHYSICS REPORTS

Low-dimensional models of coherent structures in turbulence

Philip J. Holmes[a,b], John L. Lumley[c], Gal Berkooz[c,d], Jonathan C. Mattingly[a], Ralf W. Wittenberg[a]

[a] *Program in Applied and Computational Mathematics, Princeton University, Princeton, NJ 08544, USA*
[b] *Department of Mechanical and Aerospace Engineering, Princeton University, Princeton, NJ 08544, USA*
[c] *Sibley School of Mechanical and Aerospace Engineering, Cornell University, Ithaca, NY 14853, USA*
[d] *BEAM Technologies, Inc., 110 N. Cayuga St., Ithaca, NY 14850, USA*

Received October 1996; editor: I. Procaccia

Contents

Abstract

For fluid flow one has a well-accepted mathematical model: the Navier–Stokes equations. Why, then, is the problem of turbulence so intractable? One major difficulty is that the equations appear insoluble in any reasonable sense. (A direct numerical simulation certainly yields a "solution", but it provides little understanding of the process *per se*.) However, three developments are beginning to bear fruit: (1) The discovery, by experimental fluid mechanicians, of coherent structures

PII S0370-1573(97)00017-3

in certain fully developed turbulent flows; (2) the suggestion, by Ruelle, Takens and others, that strange attractors and other ideas from dynamical systems theory might play a role in the analysis of the governing equations, and (3) the introduction of the statistical technique of Karhunen–Loève or proper orthogonal decomposition, by Lumley in the case of turbulence. Drawing on work on modeling the dynamics of coherent structures in turbulent flows done over the past ten years, and concentrating on the near-wall region of the fully developed boundary layer, we describe how these three threads can be drawn together to weave low-dimensional models which yield new qualitative understanding. We focus on low wave number phenomena of turbulence generation, appealing to simple, conventional modeling of inertial range transport and energy dissipation.

PACS: 47.27.Nz; 02.70.Dh

Keywords: Coherent structures; Karhunen–Loève decomposition; Turbulence; Symmetry; Galerkin projections; Dynamical systems

1. Introduction

In this article, we outline an approach to the construction of models of turbulent energy production which has been developed over the past 10–12 years. The methods apply to flows energetically dominated by coherent structures, and result in low-dimensional dynamical systems describing the interactions among small sets of such structures, which may then be studied via the techniques of dynamical systems theory. Analysis of the bifurcations, invariant structures and attractors in the phase spaces of these (relatively) tractable systems provides insight into physical mechanisms of turbulence production. The symmetries inherited from the original physical system and governing evolution equations play a crucial role in this enterprise.

Before introducing the tools and techniques, we prepare the scene with a brief discussion of coherent structures and the problem of turbulence in Section 2, and with an overview of the dynamical systems viewpoint in Section 3. A major tool in our analysis is the *Karhunen–Loève* or *proper orthogonal decomposition* (*POD*), which provides an empirical basis for representations of complex spatio-temporal fields that is optimal in the sense that it converges (in L^2-norm) faster on average than any other representation. We discuss this in Section 4, describing the key properties of optimality and symmetries, and the approximation of attractors. Equipped with the empirical basis, a subspace spanned by the energetically dominant *empirical eigenfunctions* can then be selected. We next project the governing equations onto this space, introduce a model to account for neglected effects due to truncation and spatial localization, and thus derive a relatively small set of ordinary differential equations (ODEs). This process is illustrated in Sections 5 and 6 for the near-wall region of the turbulent boundary layer, and a sketch of some behavior of the models thus produced is given in Section 7.

While we focus on the boundary layer application, the reader should regard it as primarily a vehicle to illustrate a more general approach. To put this work into context and suggest its broader applicability, in Section 8 we outline several other applications of low-dimensional models to turbulent and transition flows.

We then return to consider in more detail some of the behaviors revealed by the boundary layer models presented in Sections 5–7. Specifically, to appreciate and illustrate better the role of symmetry and one particular expression of it – heteroclinic cycles – that appears in some models, in Sections 9–11 we discuss symmetries in general, and the group O(2) of planar rotations and reflections in particular. We use a simpler and more accessible nonlinear scalar PDE, the Kuramoto–Sivashinsky equation, which shares some of the behaviors of the boundary layer models, to demonstrate the appearance of heteroclinic cycles in symmetric systems. In Section 12 we mention random perturbation of heteroclinic cycles, prompted by the fact that the effects of the outer flow on the near-wall region of the boundary layer models may be replaced by a quasi-random pressure field at the outer edge of that region. Finally, Section 13 contains a brief summary and discussion.

Even in the context of this review, we can merely indicate some of the key ingredients and ideas in an approach which involves several areas of applied mathematics and considerable knowledge of fluid mechanics and turbulence. For a fuller development and critical survey of this approach, we refer the interested reader to the book of Holmes et al. (1996) and the extensive literature cited therein, to which this article is heavily indebted. A shorter version of this article has also been prepared as lecture notes for a NATO Advanced Study Institute held at the Newton Institute, Cambridge, UK, in August 1995.

2. Turbulence and coherent structures

Over the last 20 or 30 years, studies of turbulent fluid motion have revealed aspects of organized motion in a wide variety of flows, i.e. there are large-scale ordered structures which, although neither steady in space nor time, persistently appear, disappear and reappear (see, for example, the articles in Lumley (1990), including Cantwell (1990), Holmes (1990) or Robinson (1991)). The "roller" structures observed by Brown and Roshko (1974) in the mixing layer provide a particularly striking example; see Fig. 1.

Flow visualization techniques and simulations have revealed *coherent structures* such as those in Fig. 1 quite clearly, but the structures typically vary considerably in space and time, and naturally their forms depend on the flow geometry and other conditions. This has made them hard to pin down, and sensitive conditional sampling techniques have been developed for their detection. Furthermore, their variability has precluded general agreement on their nature or even on a *definition* of coherent structures. However, it seems likely that such persistent macroscopic structure amidst the small-scale activity and fluctuations provides a "backbone" for many turbulent flows, and hence that *analysis of the dynamics of these structures may provide a basis for improved understanding of some aspects of turbulence*. It is this hope that motivated the studies described in the present article.

For much of this article we shall use as our illustrative example the wall region of a turbulent boundary layer. The presence of the wall leads to a structure which is strongly three-dimensional, highly intermittent and in general more complex than in free shear flows such as Fig. 1. These structures involve persistent longitudinal (streamwise) vortices and low speed "streaks", visualized via hydrogen bubble traces in Fig. 2 (Kline et al., 1967). For future reference, it is useful to establish the coordinates to be used in the wall region flow domain (see Fig. 3) in which we distinguish the homogeneous streamwise x_1, spanwise x_3, and inhomogeneous wall normal x_2 directions, with the mean flow U in the streamwise direction. The most intense motions are at a scale which is small compared to the depth of the boundary layer; this, and the fact that the range of scales present in the whole layer would demand a prohibitively high-dimensional model, provides the motivation later for artificially limiting the domain in the x_2 direction to the near-wall region. Also see Section 7.1 below. In fact, we shall take $0 \leq x_2 \leq X_2 = 40$ in the nondimensional wall units appropriate to scaling of the inner wall layer (Tennekes and Lumley, 1972; also see Section 6.3). The typical space–time evolution of the observed coherent structures is complicated, often exhibiting a repetitive cycle of events, including the lift, oscillation and ejection of longitudinal boundary layer streaks, followed

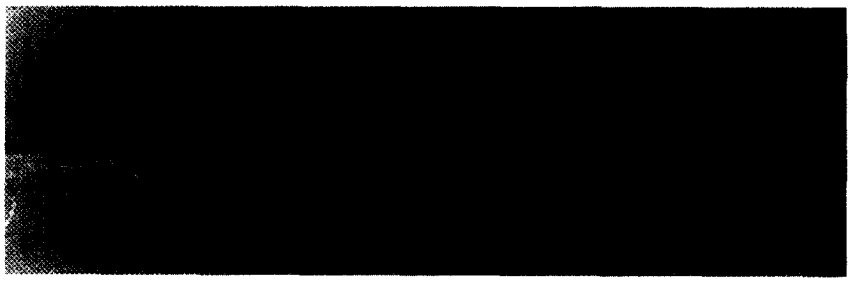

Fig. 1. A shadowgraph image of coherent structures in the turbulent mixing layer between Helium at 1015 cm/s and Nitrogen at 384 cm/s, at a pressure of 8 atm. and Reynolds number $Re \sim 10^6$. From Brown and Roshko (1974).

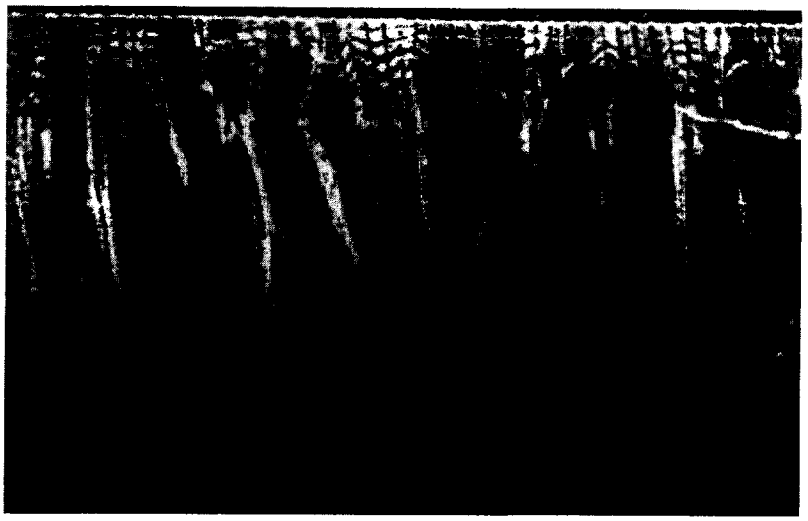

Fig. 2. Low-speed streaks visualized in the wall region of a turbulent boundary layer. Hydrogen bubbles are released into the fluid at evenly spaced intervals from a thin wire and photographed from above, looking towards the wall; the mean flow is from top to bottom. From Kline et al. (1967).

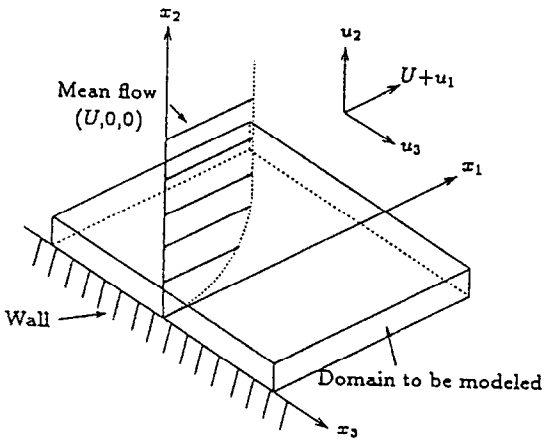

Fig. 3. The wall region: coordinates and modeling domain.

by sweep and reformation. A major characteristic activity of interest is the burst/sweep cycle, in which a "burst" of low-(streamwise-)speed fluid is forced up away from the wall ($u_1<0$, $u_2>0$), followed by a "sweep" of fast fluid moving back downward towards the wall ($u_1>0$, $u_2<0$). In this process the streaks break up and reform, often with a lateral spanwise shift. See Robinson (1991) for detailed descriptions.

We expressed above the "hope" for deeper understanding of turbulence; what goals for further understanding might one have? After all, we have a closed system of equations for incompressible flow, the Navier–Stokes equations – see (22) and (23) – which are the expressions of momentum and mass conservation in the continuum limit and which are generally believed to be an excellent model

for subsonic flows at "reasonable" temperatures and pressures. So what is the problem? It is that we cannot solve these equations in any meaningful sense for physically relevant initial conditions; in fact, a general global existence and uniqueness theory for solutions in $\mathbb{R}^3$ is still lacking (Doering and Gibbon, 1995)!

What would one seek to "explain"? There are many different scientific and technological questions pertinent to turbulence: On the one hand, one might wish to know how such complex spatial and temporally "random" motions could arise from the simple local laws of Newtonian mechanics – this may be understood, at least qualitatively, using ideas from dynamical systems theory, which was first applied to the study of turbulence by Hopf (1948) and Ruelle and Takens (1970). On the other hand, we might wish to calculate technologically important "averaged" quantities such as the drag or mixing rates in a turbulent flow. A large variety of experimental, computational and theoretical techniques has been brought to bear on questions such as these, but much remains poorly understood. We express our hope in the work described here that a well-chosen but highly simplified model, a caricature of the system, which makes use of the presence of coherent structures to choose an appropriate basis for representing velocity fields, may enable the tools of dynamical systems theory to shed new light on the problem.

3. The dynamical systems paradigm

Central to the dynamical systems viewpoint is the concept of the attractor. In brief, an attractor is an invariant, indecomposable subset of phase space which attracts solutions originating from its exterior. Characterizing a system's attractors is a significant step towards understanding its dynamics. Simply knowing that an attractor exists can be quite helpful.

The seeds of our current effort were planted by Ruelle and Takens (1970), following Hopf (1948). Their hope was to reduce the dynamics of the Navier–Stokes (NS) equations, describing (turbulent) flow, to those on an attractor, and study their bifurcations and dynamics in the context of finite-dimensional flows and maps. The NS equations are infinite-dimensional, yet in special cases, they have been shown to possess a finite-dimensional attractor, and this is believed to hold in general (Temam, 1988; Doering and Gibbon, 1995). If we could choose a subspace S_n such that the attractor, $\mathscr{A}$, and possibly other orbits asymptotic to it, formed a graph over S_n, then we could perform something akin to an inertial manifold reduction. Letting p and q be coordinates in S_n and $S_n^{\perp}$, respectively, the original system may be written as

$$\dot{p} = f(p,q)\,, \qquad \dot{q} = g(p,q)\,. \tag{1}$$

Denoting $q = h(p)$ as the graph of $\mathscr{A}$ above S_n, we can project the flow on $\mathscr{A}$ to S_n by letting $\dot{p} = f(p,h(p))$. This reduces the dimension of the system to that of S_n. The bad news for the rigorous application of such an idea is that by "finite dimensional" in the case of the Navier–Stokes equation, we indeed mean only "less than infinite". Rough estimates on the dimension are on the order of $Re^{9/4}$, which gives $\mathcal{O}(10^6$–$10^9)$ dimensions for flows of scientific and technological interest. (Here $Re = ul/\nu$ is a Reynolds number formed from the turbulent velocity, u, the "integral" or energy-containing length scale, l, and the kinematic viscosity, ν.)

Clearly a "simple" reduction to the attractor will not be sufficient to produce an ODE model of a size which might be studied analytically. Thus, we are prompted to seek, less ambitiously,

a subspace S_n which captures "most" but not all of the dynamics. In our investigations, we will take "most" to mean most of the kinetic energy on average. The naive picture we have is a conditional probability measure, $\mu(q|p)$, $p \in S_n$ and $q \in S_n^{\perp}$, sitting on the fiber Q_p above each point $p \in S_n$. Such a representation assumes the existence of a finite invariant measure for the dynamics so that the conditional distribution on the fiber above a base point is fixed in time, and can be averaged out of the dynamics in a time-independent fashion. The hope is that the behavior will be well described by the dynamics projected onto S_n, suitably augmented by the averaged effect of the neglected modes (Berkooz, 1994):

$$\dot{p} = \int_{Q_p} f(p,q)\, \mathrm{d}\mu(q|p)\,. \tag{2}$$

In the absence of detailed a priori information on invariant measures, this idea will remain a vague dream; nonetheless, bolstered with substantial physical input, it will guide our modeling of neglected effects. As we shall see, it seems essential to include some information on the neglected modes, both in wave number space and physical space, in analogy with the advantages of a center manifold, compared with a linear center eigenspace truncation.

4. The proper orthogonal decomposition

The existence of coherent structures, which contain most of the energy in certain flows, suggests that the drastic reduction in dimension postulated in the previous section might be achieved by a suitable modal decomposition which retains only these structures and appeals to averaging or modeling to account for the incoherent fluctuations. The *proper orthogonal decomposition* (POD) offers a rational way for building basis functions that emphasize such energetic features.

The POD is a procedure for extracting a basis for a modal decomposition of functions, from an ensemble of "observations" obtained experimentally or from direct numerical simulation. It is attractive in that it is a linear procedure, based on the spectral theory of compact, self-adjoint operators, so its properties and limitations are clear. Moreover, the decomposition it affords is optimal in the precise sense described below. The POD was first introduced in the context of turbulence by Lumley (1967); in other fields it is known under various alternative names, notably the *Karhunen–Loève decomposition*. See Berkooz et al. (1993) for a more general discussion, and Holmes et al. (1996) for a detailed description, including proofs of the results cited below, other applications, and some historical perspective. Also see Sirovich (1987) for a general introductory survey, and Armbruster et al. (1994) for a description of publicly available software, KLTOOL, developed for POD analysis.

The basic idea is straightforward: Suppose we have an ensemble $\{\boldsymbol{u}^k\}$ of observations (experimental measurements or numerical simulations) of a turbulent velocity field. We assume that each $\boldsymbol{u}^k$ belongs to an inner product (Hilbert) space X. Our goal is to obtain an orthogonal basis φ_j for X, so that almost every member of the ensemble can be decomposed relative to the φ_j:

$$\boldsymbol{u} = \sum_{j=1}^{\infty} a_j \varphi_j\,, \tag{3}$$

where the a_j are suitable modal coefficients. There is no a priori reason to distinguish between space and time in the definition and derivation of the empirical basis functions, but we ultimately wish to obtain a dynamical model for the coherent structures. Hence, here we shall seek spatial vector-valued basis functions φ_j, and subsequently determine the time-dependent scalar modal coefficients a_j via projection of the governing equations; giving the specific space–time decomposition

$$\boldsymbol{u}(\boldsymbol{x},t)=\sum_j a_j(t)\varphi_j(\boldsymbol{x})\,. \tag{4}$$

Here $\boldsymbol{x}\in\Omega$, where Ω denotes the spatial domain of the experiment. Typically in fluid applications, we choose the Hilbert space $X=[L^2(\Omega)]^3$ of vector-valued velocity fields, with an inner product defined by $(f,g)=\int_\Omega\sum_{i=1}^3 f_i g_i^*\,\mathrm{d}\boldsymbol{x}$. (In fact, we further restrict to the subspace of divergence free vector fields, consistent with incompressible flows.) Central to the POD is the concept of the averaging operation $\langle\cdot\rangle$, associated with a probability measure μ on X, and which is assumed to commute with the spatial integral of the L^2 inner product. The operation $\langle\cdot\rangle$ may simply be thought of as an average over a number of separate experiments, or, if we assume ergodicity, as a time average over the ensemble of observations obtained at different instants during a single experimental run.

The discussion that follows may be justified rigorously, through a careful analysis of the averaging operation and the operators involved in the POD – see Holmes et al. (1996); here we present merely an overview.

4.1. Derivation of empirical eigenfunctions

In mathematical terms, a normalized basis element φ is optimal if the average projection of $\boldsymbol{u}$ onto φ is maximized; i.e., we seek

$$\max_{\varphi\in X}\langle|(\boldsymbol{u},\varphi)|^2\rangle/\|\varphi\|^2\,, \tag{5}$$

where $|\cdot|$ denotes the modulus and $\|\cdot\|$ is the L^2-norm, $\|f\|=(f,f)^{1/2}$. This can be reformulated in terms of the calculus of variations, with a functional for the constrained variational problem

$$J[\varphi]=\langle|(\boldsymbol{u},\varphi)|^2\rangle-\lambda(\|\varphi\|^2-1)\,. \tag{6}$$

A necessary condition for extrema is the vanishing of the functional derivative for all variations $\varphi+\varepsilon\psi\in X$:

$$\frac{\mathrm{d}}{\mathrm{d}\varepsilon}J[\varphi+\varepsilon\psi]\bigg|_{\varepsilon=0}=0\,. \tag{7}$$

Some algebra, together with the fact that $\psi(\boldsymbol{x})$ is an arbitrary variation, shows that the condition (7) reduces to

$$\int_\Omega \underbrace{\langle\boldsymbol{u}(\boldsymbol{x},t)\boldsymbol{u}^*(\boldsymbol{x}',t)\rangle}_{R(\boldsymbol{x},\boldsymbol{x}')}\varphi(\boldsymbol{x}')\,\mathrm{d}\boldsymbol{x}'=\lambda\varphi(\boldsymbol{x})\,. \tag{8}$$

This is a Fredholm integral equation of the second kind whose kernel is the averaged autocorrelation tensor $R(\boldsymbol{x},\boldsymbol{x}') \stackrel{\text{def}}{=} \langle \boldsymbol{u}(\boldsymbol{x},t)\boldsymbol{u}^*(\boldsymbol{x}',t)\rangle$, which we may rewrite as the operator equation $\boldsymbol{R}\varphi = \lambda\varphi$. The optimal basis is thus given by the eigenfunctions of this integral equation. These are frequently called *empirical eigenfunctions*, since the basis is derived from the ensemble of observations $\{\boldsymbol{u}^k\}$. The operator $\boldsymbol{R}$ is clearly self-adjoint. Furthermore, under plausible conditions on the averaging measure μ, $\boldsymbol{R}$ is also compact, so that Hilbert–Schmidt theory assures us that there is a countable infinity of eigenvalues $\{\lambda_j\}$ and eigenfunctions $\{\varphi_j\}$ (which we may normalize so that $\|\varphi_j\| = 1$) given by solutions of (8). We may order the eigenvalues so that $\lambda_j \geq \lambda_{j+1}$, and by the "first", or leading, N eigenvalues (resp. eigenfunctions) we mean $\lambda_1, \lambda_2, \ldots, \lambda_N$ (resp. $\varphi_1, \varphi_2, \ldots, \varphi_N$). Note that the positive semi-definiteness of R implies that $\lambda_j \geq 0$. This representation provides a diagonal decomposition of the autocorrelation function

$$R(\boldsymbol{x},\boldsymbol{x}') = \sum_{j=1}^{\infty} \lambda_j \varphi_j(\boldsymbol{x})\varphi_j^*(\boldsymbol{x}') . \tag{9}$$

It is these empirical eigenfunctions that we use in the modal decomposition (4) above. We note that the diagonal representation (9) of the two-point correlation tensor ensures that the modal amplitudes are uncorrelated:

$$\langle a_i a_j^* \rangle = \delta_{ij}\lambda_j . \tag{10}$$

In applications, we wish only to retain eigenfunctions φ_j with strictly positive eigenvalues λ_j, i.e. those spatial structures having finite energy on average. It is natural to explore the nature of the span of these $\{\varphi_j\}$, i.e. $S = \{\sum a_j\varphi_j \mid \lambda_j > 0,\ \sum |a_j|^2 < \infty\}$: which functions can be reproduced by convergent linear combinations of these empirical eigenfunctions? It turns out that almost every member of the original ensemble $\{\boldsymbol{u}^k\}$ (with respect to the probability measure underlying the averaging operation) belongs to S. Conversely, the elements of S (including the empirical eigenfunctions) may be constructed in terms of the $\{\boldsymbol{u}^k\}$:

$$\theta \in S \Rightarrow \theta(\boldsymbol{x}) = \sum_k b_k \boldsymbol{u}^k(\boldsymbol{x}) . \tag{11}$$

The span of the eigenfunctions is thus exactly the span of all the realizations of $\boldsymbol{u}(\boldsymbol{x})$, with the exception of a set of measure zero. Frequently, these realizations do not span X (much, but not *everything* happens in turbulence); in this case, the POD eigenfunctions $\{\varphi_j \mid \lambda_j > 0\}$ do not form a *complete* basis of $[L^2(\Omega)]^3$, but rather they span only the smallest linear subspace that is sufficient to describe the observed phenomena – "you can only describe what you have seen before". Inclusion of all generalized eigenfunctions of $\boldsymbol{R}$ with zero eigenvalues gives a complete basis, but in this completion one loses the major advantage of the POD: the possibility of a drastic reduction in the dimensionality of the system.

Note that from (11), one sees that properties common to all velocity fields $\boldsymbol{u}$ in the ensemble are inherited by the empirical eigenfunctions. In incompressible fluid flows, this means in particular that the φ_j satisfy the same linear boundary conditions as the velocity field, and are divergence free. As we shall see below, symmetries also pass onto the φ_j.

4.2. Optimality

Suppose we have an ensemble member $\boldsymbol{u}(\boldsymbol{x},t)$, decomposed with respect to an (arbitrary) orthonormal basis $\{\psi_j\}$,

$$\boldsymbol{u}(\boldsymbol{x},t)=\sum_j b_j(t)\psi_j(\boldsymbol{x})\,. \tag{12}$$

Using the orthonormality of the ψ_j, from the above expression, twice the average kinetic energy per unit mass over the experiment is given by

$$\int_\Omega \langle \boldsymbol{u}\boldsymbol{u}^*\rangle \,\mathrm{d}\boldsymbol{x}=\sum_j \langle b_j(t)b_j^*(t)\rangle\,. \tag{13}$$

Hence, $\langle b_j b_j^*\rangle$ (no sum implied) represents twice the average kinetic energy in the jth mode. It follows that for the particular case of the POD decomposition (4), the energy in the jth mode is λ_j, as claimed in (10).

We may now state an optimality result for the POD: For any N, the energy in the first N modes in a proper orthogonal decomposition is at least as great as that in any other N-dimensional projection:

$$\|\boldsymbol{u}_N\|^2=\sum_{j=1}^{N}\langle a_j a_j^*\rangle=\sum_{j=1}^{N}\lambda_j\geq\sum_{j=1}^{N}\langle b_j b_j^*\rangle\,. \tag{14}$$

This follows from a result on general linear self-adjoint operators (Temam, 1988): the sum of the first N eigenvalues of $\boldsymbol{R}$ is greater than or equal to the sum of the diagonal terms in any N-dimensional projection of $\boldsymbol{R}$. Eq. (14) implies that, among all *linear* decompositions, the POD is the most efficient for modeling or reconstructing a signal $\boldsymbol{u}(\boldsymbol{x},t)$, in the sense of *capturing, on average, the most kinetic energy possible for a projection on a given number of modes*. This observation furnishes the motivation for the use of the POD in low-dimensional modeling of coherent structures. The rate of decay of the λ_j gives an indication of how fast finite-dimensional representations converge on average, and hence how well specific truncations might capture these structures.

One can, of course, define optimal bases with respect to norms other than the L^2 norm. Alternative choices of norm would simply weight characteristics other than the kinetic energy. For instance, an H^1 Sobolev norm would give a basis better adapted to capturing dissipation ($\|\nabla\boldsymbol{u}\|^2$) or vorticity ($\nabla\times\boldsymbol{u}$).

4.3. Symmetries in the POD

As indicated above, the empirical eigenfunctions inherit properties shared by all observations $\boldsymbol{u}^k$, including symmetries. For our purposes, the most important symmetry is spatial *homogeneity*. This is the condition that the averaged two-point correlation be translation invariant, i.e. it depends only on the difference between coordinates: $R(x,y)=R(x-y)$. Translation invariance can occur in spatially unbounded as well as periodic systems. Furthermore, a system may be homogeneous in some directions and not in others. It is additionally important to recognize that, while the ensemble of realizations $\{\boldsymbol{u}^k\}$ may be translation invariant on average, individual realizations typically are not.

Homogeneity is useful because in the homogeneous directions, the empirical eigenfunctions are simply Fourier modes: $\varphi_k(x) \propto e^{ikx}$. This is readily verified by substituting this *Ansatz* for the eigenfunctions into the definition (8) in the homogeneous directions, for an unbounded or periodic domain Ω:

$$\int_\Omega R(x-y)e^{iky}\,dy = \int_\Omega R(\eta)e^{ik(x-\eta)}\,d\eta = \left(\int_\Omega R(\eta)e^{-ik\eta}\,d\eta\right)e^{ikx} \stackrel{\text{def}}{=} \tilde{\lambda}_k e^{ikx}\,. \tag{15}$$

Hence, e^{ikx} is indeed an eigenfunction, with eigenvalue $\tilde{\lambda}_k$; the eigenvalues being given by the Fourier transform of the averaged autocorrelation. (Note that this indexing of the eigenvalues, by their Fourier mode number, does not necessarily correspond to the ordering in decreasing magnitude which we introduced earlier; an analysis of the spectrum may show that a mode higher than the first contains the most energy. This occurs, for instance, in the Kuramoto–Sivashinsky equation, to be discussed in Section 11, and in the spanwise direction of the boundary layer – see Fig. 4. For consistency with our previous notation, we may reorder by introducing a permutation, $j \to k(j)$, so that $\lambda_j \equiv \tilde{\lambda}_{k(j)}$, and $\lambda_j \geq \lambda_{j+1}$.)

The *continuous* symmetry of homogeneity, or translational invariance, is only one of many symmetries that fluids may exhibit, depending on the experimental setup. A given system could be invariant under *discrete* symmetries, such as translations through multiples of some finite length, or discrete rotations, for example. Such discrete symmetries would occur in a boundary layer treated with riblets – strakes parallel to the mean flow direction. In Sections 9 and 10 we shall investigate in greater depth the effect of translation and reflection symmetries on the dynamical behavior of the system.

4.4. Approximating attractors

In implementing the POD for low-dimensional modeling, we project the governing infinite-dimensional evolution equation, such as the NS equations, onto a finite-dimensional empirical subspace, of possibly quite low dimension. The question naturally arises: How well does this truncation and projection approximate the attractor of the original dynamical system?

For insight into this question, we appeal to an elementary inequality from probability theory, which gives an upper bound on the frequency of departures from the mean:

Chebyshev's inequality: *Let* $\boldsymbol{x}$ *be a vector-valued random variable, with mean* $\langle \boldsymbol{x} \rangle$ *and variance* $\sigma^2 = \langle |\boldsymbol{x} - \langle \boldsymbol{x} \rangle|^2 \rangle$. *Then for any* $\varepsilon > 0$,

$$P\{|\boldsymbol{x} - \langle \boldsymbol{x} \rangle| \geq \varepsilon\} \leq \sigma^2/\varepsilon^2\,. \tag{16}$$

We may use this inequality to estimate the probability of the system evolution remaining close to a finite-dimensional subspace spanned by the first n empirical eigenfunctions, $S_n = \text{span}\{\varphi_1, \ldots, \varphi_n\}$. The projection onto the first n modes belongs to S_n; to estimate the error incurred by neglecting the remaining modes, we examine the infinite "tail". To do this, we define an infinite-dimensional "slab" of thickness 2ε around S_n,

$$S_n(\varepsilon) = \left\{ u \in L^2(\Omega) \,\middle|\, \sum_{m=n+1}^{\infty} |(u, \varphi_m)|^2 < \varepsilon \right\}\,,$$

and let $W_n(\varepsilon)=L^2(\Omega)\backslash S_n(\varepsilon)$ denote the rest of phase space. To apply Chebyshev's inequality to estimate the fraction of time spent in $S_n(\varepsilon)$ by solutions $\boldsymbol{u}(\boldsymbol{x},t)=\sum_m(\boldsymbol{u},\varphi_m)\varphi_m=\sum_m a_m\varphi_m$, we let $\boldsymbol{y}_n$ denote the vector-valued random process

$$\boldsymbol{y}_n(t)=\{(\boldsymbol{u},\varphi_m)\}_{m=n+1}^{\infty}.$$

Then we have $\langle \boldsymbol{y}_n\rangle=0$ and $\sigma^2(\boldsymbol{y}_n)=\sum_{m=n+1}^{\infty}\langle a_m a_m^*\rangle=\sum_{m=n+1}^{\infty}\lambda_m$ (from (10)), and therefore, by Chebyshev's inequality,

$$P\{\boldsymbol{u}\notin S_n(\varepsilon)\}=P\{\boldsymbol{u}\in W_n(\varepsilon)\}=P\{\,|\boldsymbol{y}_n|\geq\varepsilon\}\leq\sum_{m=n+1}^{\infty}\lambda_m/\varepsilon^2. \tag{17}$$

Now this inequality supplies a crude bound on how bad a given finite-dimensional truncation might be, but it does not yet indicate whether the solution converges onto an attractor; in particular, the expression is meaningless as $\varepsilon\to 0$ for fixed n. To get a useful convergence result, we need an estimate of the rate of decay of the residual eigenvalues in the tail, λ_n. It turns out that there is much evidence, both physical and mathematical, that the residual decays at least exponentially fast asymptotically (in the far dissipative range). Physically, viscous dissipation smooths the velocity field at high wave numbers. The mathematical basis for this is *Gevrey regularity* of solutions of the evolution equations – see Foias and Temam (1989) for results on the Navier–Stokes equations – and the uniform exponential boundedness of the appropriate averages used in the POD; cf. Berkooz (1991). These results imply that, in the limit, $\lambda_n=o(\exp(-cn))$, $c>0$; of course, these are only asymptotic results, not directly applicable to the finite- and low-dimensional modes of interest to us, where we truncate far below the far dissipative range, but they do provide a guide.

Equipped with the exponential decay of the empirical eigenvalues, we may then choose a sequence of $\varepsilon_n\to 0$ so that additionally

$$\sum_{m=n+1}^{\infty}\lambda_m/\varepsilon_n^2\to 0\quad\text{as }\varepsilon_n\to 0;$$

for instance, we may take $\varepsilon_n=o(\exp(-dn))$, for some $d<c/2$. This choice gives us a sequence of slabs $S_n(\varepsilon)$ with thickness going exponentially to zero, while the probability that the solution is in the slab, goes exponentially to one. In this picture, we have an attractor which is very thin, even though very high or even infinite-dimensional. The thinning slabs capture more and more of the energy as we include more modes, and it is reasonable to postulate that the dynamics is controlled by a finite number of modes; this forms the basis for our work. Note that the above attractor may not be compact; however, it is possible to show that with exponential decay of the empirical eigenvalues, practically all the support of the invariant measure of the dynamics *is* contained in a compact set. For a further introductory discussion of these regularity results, see Berkooz et al. (1993). A fuller discussion of the POD, describing several other properties and applications, is given in Holmes et al. (1996).

5. Representation of boundary layer flows

The previous section provided a theoretical foundation for projection onto an orthonormal set of empirical eigenfunctions. We now describe how this is carried out in practice in a specific case.

A set of data is required in order to obtain the averaged autocorrelation tensor $R(\boldsymbol{x},\boldsymbol{x}')$, whose eigenfunctions form the POD basis. The data could be experimental or numerical; the larger the data set, the better the statistics. The original study of Aubry et al. (1988) used eigenfunctions derived from experiments conducted by Herzog (1986) at Penn State, in a circular pipe at Reynolds number $Re\sim 6750$, based on centerline velocity. Later studies used data sets obtained numerically by Moin and Moser (1989) and Moin (1984), for direct numerical simulations of channel flow at $Re\sim 3$–4000, and large eddy simulations at $Re\sim 13\,800$. Typically, experimental data sets are well resolved in terms of time averages, but may have poor spatial resolution; numerical data are well resolved spatially, but often too brief for good temporal statistics.

In the data ensembles used in the work described below, the mean velocity $\boldsymbol{U}$ is subtracted at the outset (cf. Fig. 3). Thus, $\{\boldsymbol{u}^k\}$, $R(\boldsymbol{x},\boldsymbol{x}')$ and the empirical bases φ_j produced represent the zero mean turbulent fluctuations alone. This removal of $\boldsymbol{U}$ is consistent with the decomposition of the full velocity field described in Section 6.

5.1. Symmetries of the empirical eigenfunctions

All of these data sets exhibit certain symmetries, which consequently carry over to the empirical eigenfunctions. In particular, the fully developed boundary layer, in either channel or pipe, is translation invariant[1] (on average) in the streamwise and spanwise directions, and reflection invariant in the spanwise direction. The meaning of "on average" is that, while individual realizations of the velocity field are typically not translation or reflection invariant (coherent structures occur *somewhere*), averaging over a sufficiently large ensemble does yield an autocorrelation tensor with that symmetry. In the light of the discussion in the previous section, this implies that the POD eigenfunctions in those directions are Fourier modes, and may be labelled by their Fourier wave numbers. Indeed, translation invariance implies that $R(x_1,x_1',x_2,x_2',x_3,x_3') = R(x_1 - x_1', x_2, x_2', x_3 - x_3')$, where x_1 denotes the streamwise, x_2 the wall normal and x_3 the spanwise direction (recall Fig. 3). We may thus work with the power spectrum, and take the (discrete) Fourier transform of R in the 1 and 3 directions (over domains of lengths L_1 and L_3, respectively) to give $\hat{R}(k_1,k_3;x_2,x_2')$. It is $\hat{R}$ whose eigenfunctions provide the empirical basis, $\boldsymbol{\phi}_n(k_1,k_3;x_2) \equiv \boldsymbol{\phi}^{(n)}_{k_1k_3}(x_2)$, the corresponding eigenvalues $\lambda^{(n)}_{k_1k_3}$ describing the average energy content in each eigenfunction family (n), at each Fourier wave number pair (k_1,k_3). The domain size in the normal direction is X_2, and the eigenfunctions satisfy the orthonormality condition

$$(\boldsymbol{\phi}^{(m)}_{k_1k_3}, \boldsymbol{\phi}^{(n)}_{k_1k_3}) = \int_0^{X_2} \phi^{(m)}_{i_{k_1k_3}}(x_2)\phi^{(n)*}_{i_{k_1k_3}}(x_2)\,\mathrm{d}x_2 = \delta_{mn}\,,$$

where ϕ_i is the ith component of $\boldsymbol{\phi}$, and summation over i is assumed.

Fig. 4 shows the dependence of the empirical eigenvalues on spanwise Fourier wave number, derived from the data of Herzog (1986). The peak corresponds to the average streak spacing seen in Fig. 2. In the streamwise direction, the spectrum is peaked at $k_1 = 0$, indicating considerably longer scales in this direction. We will draw on this empirical eigenvalue spectrum in choosing specific truncations, below.

[1] In the case of pipe flow, "spanwise translation" corresponds to rotation about the axis.

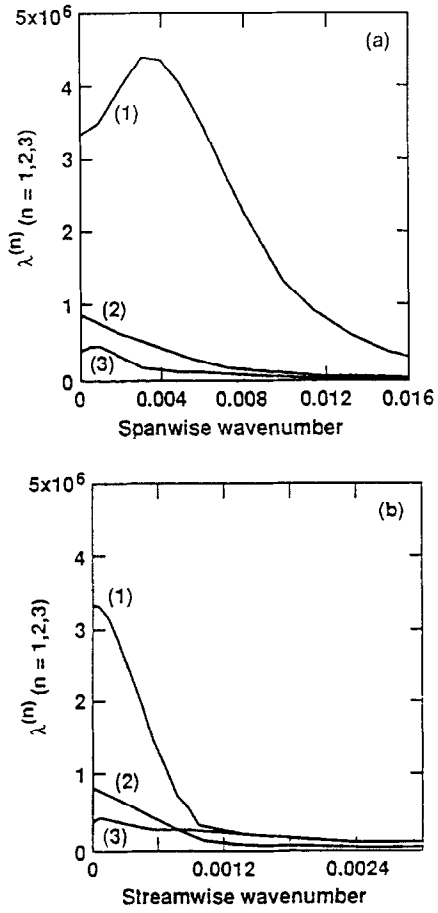

Fig. 4. Empirical eigenvalue spectra for the near wall region: $\lambda^{(n)}$ as a function of (a) spanwise wave number k_3/L_3, (b) streamwise wave number k_1/L_1. From Herzog (1986).

In addition to translation invariance, the eigenfunctions $\phi(x_2)$ inherit other symmetries from those in the experimental or numerical two-point correlation tensor (see Section 4.3). In particular, when taken together with the Fourier modes, the eigenfunctions are divergence-free; furthermore, there is reflection symmetry about a midplane in the spanwise direction, and the entries of the tensor are real. In terms of the eigenfunctions, these last two symmetries imply

$$\begin{aligned}
\boldsymbol{\phi}^{(n)}_{-k_1 k_3} &= (\phi^{(n)*}_{1_{k_1 k_3}}, \phi^{(n)*}_{2_{k_1 k_3}}, -\phi^{(n)*}_{3_{k_1 k_3}}), \\
\boldsymbol{\phi}^{(n)}_{k_1 - k_3} &= (\phi^{(n)}_{1_{k_1 k_3}}, \phi^{(n)}_{2_{k_1 k_3}}, -\phi^{(n)}_{3_{k_1 k_3}}), \\
\boldsymbol{\phi}^{(n)}_{-k_1 - k_3} &= (\phi^{(n)*}_{1_{k_1 k_3}}, \phi^{(n)*}_{2_{k_1 k_3}}, \phi^{(n)*}_{3_{k_1 k_3}}).
\end{aligned} \tag{18}$$

Consistent with the observations and empirical eigenfunctions derived from them, the NS equations (with periodic boundary conditions in the x_1 and x_3 directions) themselves display the same symmetries, namely equivariance under translations and reflections in the spanwise direction and translation

in the streamwise direction:

$$x_3 \mapsto x_3 + \zeta_3\,, \qquad x_3 \mapsto -x_3\,, \qquad x_1 \mapsto x_1 + \zeta_1\,. \tag{19}$$

5.2. The modal expansion

In terms of the eigenfunction expansion (4), the eigenfunctions $\varphi_n(\boldsymbol{x})$ thus consist of Fourier modes in the x_1 and x_3 directions, and the above functions $\phi^{(n)}_{k_1k_3}$ in the x_2 direction. The index n represents a *family* of empirical eigenfunctions, for different values of k_1 and k_3 (the energy of a family of eigenfunctions is derived by summation over the wave numbers k_1 and k_3). The full expansion, in the form (4), for the ith component of the velocity field (where $i=1,2,3$) is thus

$$u_i(x_1,x_2,x_3,t) = \frac{1}{\sqrt{L_1L_3}} \sum_{n=1}^{\infty} \sum_{\substack{k_1=-\infty \\ k_3=-\infty}}^{\infty} a^{(n)}_{k_1k_3}(t) e^{2\pi i((k_1/L_1)x_1+(k_3/L_3)x_3)} \phi^{(n)}_{i_{k_1k_3}}(x_2)\,. \tag{20}$$

The symmetry (18) implies for the modal coefficients

$$a^{(n)}_{k_1k_3} = a^{(n)*}_{-k_1-k_3}\,, \tag{21}$$

guaranteeing reality of the velocity field.

After substituting (20) for the velocity field into the Navier–Stokes equations, truncating at some finite number of modes $n=N$, $k_1=\pm K_1$, $k_3=\pm K_3$, and taking the inner product with each included mode in turn, we obtain a finite system of ODEs for the amplitudes $a^{(n)}_{k_1k_3}(t)$. It is this system that we derive in the next section, and whose properties we shall subsequently study. We will consider specific choices for length scales L_j and truncation wave numbers K_j, N in Section 7.

6. Projection of the Navier–Stokes equations and modeling

We first rewrite the NS equations in a type of Reynolds decomposition that isolates the dynamics of coherent structures and their interaction with the mean flow; both the neglected (high) wave number modes and the mean flow are modeled. Next, we project the NS equations onto the empirically obtained family of subspaces, using a Galerkin projection. Lastly, we truncate the system – in fact, rather drastically – in order to obtain a finite- and low-dimensional system that is amenable to analysis and understanding. Several assumptions are necessary in the projection process, and they will be touched on and justified here briefly; the reader should refer to Holmes et al. (1996) for more details.

We begin with the incompressible Navier–Stokes (NS) equations without body forces, for the fluid velocity field $\boldsymbol{v}(\boldsymbol{x},t)$ and pressure field $\pi(\boldsymbol{x},t)$:

$$\boldsymbol{v}_t + \boldsymbol{v}\cdot\nabla\boldsymbol{v} = -(1/\rho)\nabla\pi + \nu\nabla^2\boldsymbol{v}\,, \tag{22}$$

$$\nabla\cdot\boldsymbol{v} = 0\,. \tag{23}$$

We choose periodic boundary conditions in the streamwise and spanwise directions, i.e. on $x_1=0, L_1$ and $x_3=0$, L_3, no slip boundary conditions on the wall, that is $\boldsymbol{v}=0$ on $x_2=0$, and an as yet unknown boundary condition $\boldsymbol{v}=\boldsymbol{f}(x_1,x_3,t)$ on the upper edge of the wall layer $x_2=X_2$.

6.1. Reynolds decomposition

We first perform the Reynolds decomposition of the fluid into a mean flow and a fluctuating field, $\boldsymbol{v} = \boldsymbol{U} + \boldsymbol{u}$, $\pi = P + p$, where $\boldsymbol{U} \equiv \langle \boldsymbol{v} \rangle_s$ and $P \equiv \langle \pi \rangle_s$ are spatially averaged quantities in the x_1, x_3 directions; for instance,

$$\boldsymbol{U}(x_2, t) = \langle \boldsymbol{v} \rangle_s = \frac{1}{L_1 L_3} \int_0^{L_1} \int_0^{L_3} \boldsymbol{v}(x_1, x_2, x_3, t)\, \mathrm{d}x_1\, \mathrm{d}x_3 .$$

If L_1 and L_3 are large enough, the mean flow $\boldsymbol{U} = U(x_2, t)\boldsymbol{e}_1$ is in the streamwise x_1 direction, and has a slow enough time dependence that we can neglect $\boldsymbol{U}_t$ relative to $\boldsymbol{u}_t$.

Averaging (22), we obtain the equation for the mean flow,

$$\boldsymbol{U}_t + \boldsymbol{U} \cdot \nabla \boldsymbol{U} + \langle \boldsymbol{u} \cdot \nabla \boldsymbol{u} \rangle_s + (1/\rho) \nabla P - \nu \nabla^2 \boldsymbol{U} = 0 , \tag{24}$$

where $\langle \boldsymbol{u} \cdot \nabla \boldsymbol{u} \rangle_s$ is the Reynolds stress term. Subtracting the mean equation (24) from (22), we obtain an evolution equation for the turbulent fluctuations,

$$\boldsymbol{u}_t + \boldsymbol{U} \cdot \nabla \boldsymbol{u} + \boldsymbol{u} \cdot \nabla \boldsymbol{U} + \boldsymbol{u} \cdot \nabla \boldsymbol{u} - \langle \boldsymbol{u} \cdot \nabla \boldsymbol{u} \rangle_s + (1/\rho) \nabla p - \nu \nabla^2 \boldsymbol{u} = 0 . \tag{25}$$

Noting that $\boldsymbol{U} \cdot \nabla \boldsymbol{U} = 0$, and assuming $\boldsymbol{U}_t \approx 0$ and that streamwise and spanwise variations of mean quantities are negligible, we may obtain an approximation for the Reynolds stress from (24), in component form,

$$\langle u_{i,j} u_j \rangle_s = -(1/\rho) P_{,i} + \nu U_{,22} \delta_{i1} , \tag{26}$$

where the comma denotes partial differentiation, for instance, $u_{i,j} \equiv \partial u_i / \partial x_j$ and $U_{,22} \equiv \partial^2 U / \partial x_2^2$.

6.2. The mean flow

In order to close the equations for $\boldsymbol{u}$, we need to model the mean flow in some way. In Aubry et al. (1988), the mean flow was expressed as a balance between the effects of pressure and those of the coherent structures. Similar strategies have been adopted for other flows, see Section 8. Order of magnitude estimates, which may be justified by asymptotic calculations through manipulation of the first and second components of (26), give

$$U(x_2, t) = \frac{1}{\nu} \int_0^{x_2} \langle u_1 u_2 \rangle_s (x_2', t)\, \mathrm{d}x_2' + (u_\tau^2 / \nu)(x_2 - x_2^2 / 2H) ; \tag{27}$$

see Holmes et al. (1996) or Berkooz et al. (1993b). Here the first term on the right-hand side is due to the feedback from the turbulent bursts into the "locally averaged" mean flow that cause U to collapse as $\langle u_1 u_2 \rangle_s$ undergoes a (negative) Reynolds stress burst, while the second term is a "constant" driving term corresponding to the mean pressure gradient. Here u_τ is the friction velocity giving a measure of the shear stress at the wall, defined by $u_\tau^2 = \nu \partial U / \partial x_2 |_{x_2 = 0}$, and we assume $x_2 \ll H$, where H is half the width of the channel. Substitution of (27) into the full Eqs. (25) yields a closed system amenable to further analysis. An important property is that the first part of the expression for the mean flow gives rise to a cubic term in the full system, which implies global stability for the final dynamical system. Early studies (Aubry, 1986, unpublished) with a constant mean profile $\boldsymbol{U}(x_2)$ showed that solutions of (25) typically grew without bound.

The key idea in deriving the feedback model of (27) is that, while the model domain $[0,L_1]\times[0,L_3]$ should be large enough in the streamwise and spanwise directions that the assumptions on unidirectionality of $\boldsymbol{U}$ and magnitude of $\boldsymbol{U}_t$ in Section 6.1 hold, it must also be small enough that relatively few basis functions are required to capture the bulk of the turbulent energy. This size limitation implies that the time dependence of the mean $\boldsymbol{U}=\langle \boldsymbol{u}\rangle_s(x_2,t)$ cannot be neglected: as the initial studies noted above indicated, for realistic energy input it must be allowed to respond to local turbulent activity in the domain.

6.3. Losses to neglected modes and normalization

The next step in the analysis is to take account of the fact that we will be performing a rather violent truncation, only retaining modes that are linearly unstable or weakly stable, without keeping "stable" modes that are nevertheless dynamically active. With this drastic truncation the energy cascade mechanism that forms the basis for the turbulent energy transfer from long to short wavelength modes is lost, and must be modeled; otherwise, the overall energy balance, in which the small-scale turbulent motions act as energy sinks for the coherent structures, is upset. To obtain such a model, we further decompose the turbulent velocity field into resolved components $\boldsymbol{u}_<$, representing the coherent structures, and unresolved smaller scale components $\boldsymbol{u}_>$: $\boldsymbol{u}=\boldsymbol{u}_<+\boldsymbol{u}_>$; and we project Eq. (25) (with (27)) onto the subspace of resolved components. Once again, in order to have a closed system, we need to model the small-scale $\boldsymbol{u}_>$ in terms of the larger scales $\boldsymbol{u}_<$. For this, we use a Heisenberg spectral transfer model, or eddy viscosity mechanism; for details, see Holmes et al. (1996, Ch. 9). In the modeling, two "free" parameters α_1 and α_2 are introduced, which should both be of order one, but which can be adjusted to obtain the appropriate energy flow to the unresolved modes (cf. (28) below). These parameters (which, for simplicity, are later equated) lead to a bifurcation parameter in the dynamical system model.

Before writing down the restricted partial differential equation for the resolved modes (the coherent structures), we normalize the equations using wall units. That is, given the friction velocity u_τ and viscosity ν, the units of length, time and velocity are ν/u_τ, ν/u_τ^2 and u_τ, respectively; the unit of pressure is ρu_τ^2, and we denote normalized pressure by p^τ. In such wall variables, all wall bounded flows with the same pressure gradient look the same; in particular, the Reynolds number in wall units is unity, so that viscosity does not appear in the normalized equations. Thus, using (27) in (25) and employing the Heisenberg model, the evolution equations for the coherent structures become

$$\begin{aligned}\frac{\partial u_i}{\partial t} &= -u_{i,1}\left[\int_0^{x_2}\langle u_1u_2\rangle_s\,\mathrm{d}x_2'+\left(x_2-\frac{x_2^2}{2H}\right)\right]-u_2\,\delta_{i,1}\left[\langle u_1u_2\rangle_s+\left(1-\frac{x_2}{H}\right)\right]\\ &\quad+(1+\alpha_1\nu_T)u_{i,jj}-[(u_{i,j}u_j)-\langle u_{i,j}u_j\rangle_s]+\tfrac{1}{3}\alpha_2 l_>^2[(u_{k,l}+u_{l,k})(u_{k,l}+u_{l,k})\\ &\quad-\langle(u_{k,l}+u_{l,k})(u_{k,l}+u_{l,k})\rangle]_{,i}-p^\tau_{,i}\,.\end{aligned}\tag{28}$$

Here ν_T and $l_>$ are a viscosity and length scale characteristic of the unresolved modes, which are model parameters implicitly dependent on the domain size and wave number cutoff; we omit the subscript $<$ on $\boldsymbol{u}_<$.

6.4. Galerkin projection

We now perform Galerkin projection onto the empirical subspace S_n, substituting the modal decomposition (20) into (28). In this there are two steps: Fourier transformation in the x_1, x_3 directions, followed by taking the inner product with the empirical eigenfunction $\phi^{(n)}_{k_1 k_3}(x_2)$. The details for the Galerkin projection, and the considerable algebra involved, are omitted here; see Holmes et al. (1996) for explicit expressions and numerical values for the coefficients. The process of Galerkin projection will be described in more detail for the far simpler case of the Kuramoto–Sivashinsky equation in Section 11.

The final result of this process is a system of the form

$$\dot{\boldsymbol{a}} = [\boldsymbol{A}_1 + (1 + \alpha_1 \nu_T)\boldsymbol{A}_2]\boldsymbol{a} + [\boldsymbol{Q}_1(\boldsymbol{a},\boldsymbol{a}) + \tfrac{2}{3}\alpha_2 l_>^2 \boldsymbol{Q}_2(\boldsymbol{a},\boldsymbol{a})] + \boldsymbol{C}(\boldsymbol{a},\boldsymbol{a},\boldsymbol{a}) + \xi(t)\,, \tag{29}$$

where $\boldsymbol{a}$ denotes the vector of modal coefficients $a^{(n)}_{k_1,k_3}(t)$, and the terms $\boldsymbol{A}_j\boldsymbol{a}$, $\boldsymbol{Q}_j$ and $\boldsymbol{C}$ are, respectively, linear, quadratic and cubic terms in $\boldsymbol{a}$.

6.5. The pressure term

Of particular interest here is the additive "forcing" $\xi(t)$, which represents a boundary pressure term. In typical projections of the Navier–Stokes equations on divergence-free bases, the pressure gradient is eliminated by integration by parts, but in our case an unusual boundary condition is applied in the wall normal direction – a spatial cutoff at $X_2 = 40$ wall units, quite near the wall. As noted in Section 2, to obtain a reasonably low-dimensional description, we want to model only the wall region, and so some such cut-off or weight function must be used.

We briefly indicate how the term $\xi(t)$ arises: By the divergence theorem, we have the identity for the inner product between the gradient of a scalar, ∇p, and a divergence-free vector $\boldsymbol{u}$,

$$(\nabla p, \boldsymbol{u}) = \int_\Omega \nabla p \cdot \boldsymbol{u}\, \mathrm{d}\boldsymbol{x} = \int_{\partial\Omega} \boldsymbol{n} \cdot (p\boldsymbol{u})\, \mathrm{d}S\,,$$

where $\boldsymbol{n}$ denotes the unit normal on the boundary $\partial\Omega$ of the domain Ω. In the present case, after Fourier transformation and projection onto the empirical eigenfunctions, which are also divergence-free, we have

$$\begin{aligned}(\nabla p, \boldsymbol{\phi}) &= \int_0^{L_1}\int_0^{X_2}\int_0^{L_3} \nabla p \cdot \boldsymbol{\phi}\, \mathrm{d}x_3\, \mathrm{d}x_2\, \mathrm{d}x_1 \\ &= \int_0^{X_2}\int_0^{L_3} p\phi_1\, \mathrm{d}x_3\, \mathrm{d}x_2\Big|_0^{L_1} + \int_0^{L_1}\int_0^{L_3} p\phi_2\, \mathrm{d}x_3\, \mathrm{d}x_1\Big|_0^{X_2} \\ &\quad + \int_0^{L_1}\int_0^{X_2} p\phi_3\, \mathrm{d}x_2\, \mathrm{d}x_1\Big|_0^{L_3}\,. \end{aligned} \tag{30}$$

The first and third terms on the right-hand side cancel identically because of periodic boundary conditions in the x_1, x_3 directions, while the middle term at $x_2 = 0$ also vanishes, since the empirical eigenfunctions satisfy the no-slip condition at the wall. However, the remaining term survives, as the empirical eigenfunctions do not vanish on the upper edge of the wall region. The normalized pressure term thus transforms as

$$p^\tau \to \int_0^{L_1} \int_0^{L_3} p\phi_2 \, dx_3 \, dx_1 \Big|_{x_2 = X_2} = \hat{p}^\tau_{k_1 k_3}(X_2)\phi^{(n)*}_{2_{k_1 k_3}}(X_2) \,. \tag{31}$$

Note that in the projection process the (unspecified) velocity boundary condition $\boldsymbol{v}|_{x_2 = X_2} = \boldsymbol{f}(x_1, x_3, t)$ has been replaced by a scalar pressure field $\hat{p}^\tau$.

The conditions at this boundary are still not specified within the model, but must be estimated or supplied from independent computations. However, the presence of this pressure term is a potentially useful feature of the model, since the pressure field at $x_2 = X_2$ represents communication between the modeled wall layer and the outer region of the flow; as such, one can compare results obtained when it is present and absent, and hence distinguish between inner and outer influences on the dynamics in the wall layer. (Note that the quadratic pseudo-pressure term $\boldsymbol{Q}_2$ also arises due to the "free surface", and would vanish otherwise; however, it is small compared to $\boldsymbol{Q}_1$ and its effects may often be neglected.)

Replacement of a vectorial velocity boundary condition by a scalar appears to contradict requirements for well-posedness of the PDE (28) (Zhou and Sirovich, 1992), but as argued by Berkooz et al. (1995, unpublished), it can be shown that, if an inertial manifold exists, then specification of pressure boundary conditions does indeed result in a well-posed problem. (The proof relies on studies of finite-dimensional representations of the flow on the inertial manifold.) See Holmes et al. (1996, Section 12.4) for more information.

A simple approach to modeling the pressure field is to replace $\xi(t)$ by small additive random excitations characteristic of disturbances in the outer layer. Order of magnitude estimates indicate that typically $|\xi_i/a_i| \sim \mathcal{O}(10^{-2})$, so that to a first approximation one can ignore such an additive random term. Later in Section 12, the effect of noise will be included, and we shall be able to distinguish between inner and outer layer effects and see that the term $\xi(t)$ may play an important role.

7. Structure and some solutions of the models

In the previous section, we outlined the Galerkin projection, which yields a system of ordinary differential equations from the NS equations. This process in fact produces a nested hierarchy of models, containing increasing numbers of modes, as one seeks to approximate a lesser or greater fraction of the average energy by choosing L_1, L_3, X_2 and K_1, K_3, N in the truncated representation (20) appropriately. One must balance the inclusion of more modes, which implies a better representation of the velocity field (in terms of energy captured), with increasing dimension, which renders the ODEs more unwieldy, analytically complicated, and opaque. Ideally, we would like to study systems that are as small as possible, but will still yield relevant results.

7.1. Choice of truncation

With this in mind, the original system studied (Aubry et al., 1988) was a severe truncation which incorporated only a single family of eigenfunctions ($N=1$) and a single streamwise Fourier mode ($K_1=0$); i.e. the velocity fields have no streamwise dependence. In the spanwise direction, up to $K_3=8$ modes were initially included, although almost all studies were done with $K_3=5$. The reasons for this choice and the choice of length scales L_1, L_3 and X_2, were the following.

We wish to reproduce the cross-stream interactions that contribute to the observed turbulent bursts. It appears that a spanwise domain length of $L_3=333$ and five nonzero modes ($K_3=5$) can achieve this, being large enough to permit the interaction between two eddy pairs that lead to bursts. One must certainly include wave numbers characteristic of the spanwise energy spectrum exhibited by the empirical eigenvalues, with one near the peak and enough "interstitial" wave numbers to afford realistic interactions; see Fig. 4.

In the streamwise direction, the eigenvalue spectrum as a function of streamwise wave number peaks at the origin, indicating a long recurrence period for coherent structures in the streamwise direction. It thus seems plausible to consider at first coherent structures with no streamwise variation, and it hence does not matter how long the domain is in that direction ($L_1=333$ was chosen by Aubry et al. (1988)).

In the direction normal to the wall, a distance of $X_2=40$ in wall units was chosen. In this direction, there are the conflicting requirements of, firstly, resolving as much as possible of the coherent structures, which extend well into the flow; while, secondly, avoiding excessive complexity, as further from the wall, the range of spatial scales and consequently the number of excited degrees of freedom increases – see Moin (1984), for example. The above choice is a compromise, which permits us to retain just one family of empirical eigenfunctions for now.

Having chosen K_1, K_3 and N, we may write down the modal equations for the velocity field which, being constant in the streamwise direction, we may term "two-and-a-half-dimensional". The decomposition (20) reduces to

$$\boldsymbol{u}(\boldsymbol{x},t)=\sum_{k_3=-K_3}^{K_3} a^{(1)}_{0,k_3}(t)\mathrm{e}^{2\pi\mathrm{i}(k_3/L_3)x_3}\boldsymbol{\phi}^{(1)}_{0,k_3}(x_2)\,, \tag{32}$$

and the ODEs (29) simplify considerably; in component form they become

$$\begin{aligned}\dot{a}_k &= [A^1_k+(1+\alpha v_T)A^2_k]a_k \\ &\quad+\left[\sum_{k'} Q^1_{k\ k-k'}a_{k'}a_{k-k'}+\frac{2}{3}\alpha l^2_{>}\sum_{k'} Q^2_{k\ k-k'}a_{k'}a_{k-k'}\right] \\ &\quad+\left(\sum_{k'} C_{kk'}|a_{k'}|^2\right)a_k+\xi_k(t)\,,\end{aligned} \tag{33}$$

where $a_k\equiv a^{(1)}_{0,k_3}$, and we have set the loss parameters $\alpha_1=\alpha_2=\alpha$. That is, in this special case, the linear terms become diagonal, simplifying the analysis considerably, and the cubic terms also take a simple form. In fact, the overall structure is similar to that of the Fourier mode projections of the single space dimensional Kuramoto–Sivashinsky equation described in Section 11.

As already noted, the cubic terms are of particular importance here, as they guarantee stability. The coefficients $C_{kk'}$ turn out to be all negative, so that one can construct a Liapunov function and hence demonstrate the existence of an absorbing ball B for the dynamics. The attractor may then be found as the image of B asymptotically in time: $\mathscr{A} = \bigcap_{t\geqslant 0} \varphi_t(B)$, where φ is the dynamical evolution operator.

Specific coefficients A_k^j, $Q_{k\ k-k'}^{j}$, $C_{kk'}$ for the case $K_3 = 5$ are tabulated in the appendix of Aubry et al. (1988); however, we note that a multiplicative factor of $\sqrt{L_1 L_3}$ was inadvertently omitted from the left-hand sides of the ODEs analogous to (33) in that paper, leading to a compression of time scales by 333. This led to an erroneous interpretation of bursting timescales, which was corrected by Sanghi and Aubry (1993) without discussion of its implications. We return to this issue in Section 12.

7.2. Symmetries

Eq. (33) with the pressure term $\xi_k(t)$ set to zero (which we will assume in this section), is equivariant under the group O(2) of rotations and reflections in Fourier space, corresponding to spanwise rotations by ζ_3 and reflection. Specifically, as shown in Eqs. (36)–(39) below:

$$T_{\zeta_3}\colon\quad x_3 \mapsto x_3 + \zeta_3 \text{ becomes } T_{\zeta_3} : a_k \mapsto \mathrm{e}^{2\pi \mathrm{i}(k/L_3)\zeta_3} a_k\,, \tag{34}$$

$$R_f\colon\quad x_3 \mapsto -x_3 \text{ becomes } R_f : a_k \mapsto a_k^*\,. \tag{35}$$

Section 9 contains further discussion of symmetries; equivariance here simply means that elements of O(2) map solutions to other solutions. Note that our ODE is just the restriction of (29) to the subspace $k_1 = 0$; the symmetry under streamwise translations is not included explicitly here, since all non-zero streamwise modes have been excluded in the modal representation (32).

By reality of the vector field, we have $a_k^*(t) = a_{-k}(t)$, so that we only need to solve a set of K_3 complex ODEs, or $2K_3$ real ones. For $K_3 = 5$ we thus have a 10-dimensional model system, one that is highly truncated but, as we shall see, is still quite interesting.

It is useful to consider not only symmetries, but also invariant subspaces in this system; these provide a "backbone" for further analysis. Eq. (35) implies that the purely real subspace is invariant, as is any rotation of it under T_{ζ_3} (34). Similarly, the structure of the quadratic and cubic terms of the ODEs implies that the subspace spanned by the even Fourier modes $k = 2, 4, \ldots$ is also invariant. These lower-dimensional subspaces allow us to "parse" the system and achieve a partial understanding of its bifurcations and dynamical properties. (Note also that the $K_1 = 0$ system is invariant in higher-dimensional systems with streamwise variation having only the first family $N = 1$ of empirical eigenfunctions, so the results of the $K_1 = 0$ study are useful for later work in which $K_1 > 0$.)

7.3. Behavior of the models

The 10-dimensional model equations (33) for $K_3 = 5$ were studied by Aubry et al. (1988), and their behavior is briefly outlined here. Numerical integrations of the ODEs (33) were done using a fixed step Runge–Kutta method, and bifurcation analyses were performed on the system. The

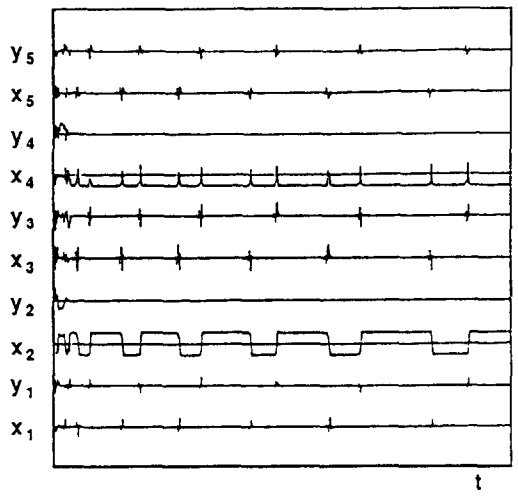

Fig. 5. Time histories of the modal coefficients, for $\alpha = 1.4$; from Aubry et al. (1988).

time-dependent amplitudes obtained from the integration were then substituted back into the expansion (32) to reconstruct time and space behavior of the velocity field as predicted by the model.

A typical result of such a simulation for the modal coefficients is given in Fig. 5 (where x_i, y_i are the real and imaginary parts of the coefficients). The corresponding reconstructed velocity field is shown in Fig. 6. Note that the solution has a characteristic repeating structure, and for most of the cycle it remains near a fixed point with only the amplitudes of the 2 and 4 modes nonzero; i.e. the dynamics remains near the invariant subspace spanned by these modes. During this time, the amplitudes of modes 1, 3 and 5 grow exponentially in an oscillatory fashion, until eventually the 2 and 4 modes respond rapidly, the phase of the 2 mode changing by π and that of the 4 mode by 2π, while the amplitudes of the 1, 3 and 5 modes simultaneously collapse to zero. The cycle then repeats. One can also see how the active unstable modes switch from the real x_1, x_3, x_5 subspace to the imaginary y_1, y_3, y_5 subspace and back again. Solutions of this type persist and appear strongly attractive over a relatively wide range of parameters, α.

What is happening here? From a consideration of the behavior in phase space, we seem to have *heteroclinic cycles* – the solution moves from the vicinity of one unstable fixed point to another and back again. In fact, analyses analogous to those sketched below for the two-mode model in Section 10 reveal that the steady 2/4 mode solutions constitute a circle of saddle points with two-dimensional heteroclinic orbits connecting diametrically opposite points. Now generically, heteroclinic cycles are structurally unstable, and can be removed by small perturbations (Guckenheimer and Holmes, 1983); yet they are observed to persist here, for general initial conditions and for ranges of parameters. This is possible, in this case, due to the symmetries of the system, which play a crucial role in stabilizing the heteroclinic cycles, as we will show in Sections 9 and 10.

Before proceeding to this, it is useful to consider the physical implications for the observed behavior: In the reconstructed velocity field (see Fig. 6) one can see clear evidence for the burst-sweep cycle that we set out to explain. That is, in spite of the extreme truncation, this 5-mode model qualitatively captures the gross features of the turbulent burst-sweep cycle in the boundary layer,

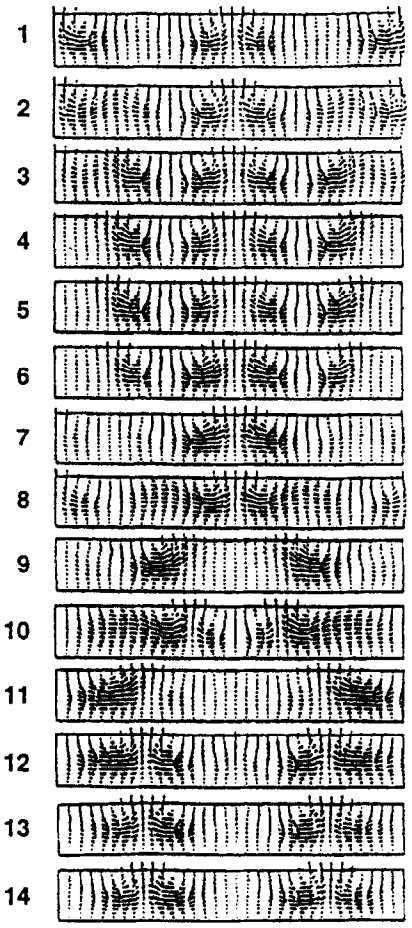

Fig. 6. Cross-stream (u_2, u_3) components of the velocity field corresponding to a single heteroclinic excursion, reconstructed from the temporal dynamics of the modal coefficients at $\alpha = 1.4$, shown in Fig. 5. From Aubry et al. (1988).

including the lateral shift in the position of vortices. The evidence strongly suggests that this cycle corresponds to a heteroclinic cycle in phase space, with the mechanism driving the bursts being the excitation of an unstable mode involving spanwise wave numbers 1, 3 and 5.

Eqs. (33) were simulated over a range of loss parameter values, α (high α implies high-energy transfer to neglected modes). The bifurcation diagram is shown in Fig. 7. For decreasing α, we find a globally stable equilibrium (in the 2, 4 subspace) becoming unstable to give various types of mixed mode solutions, including two "windows" of heteroclinic cycles, and travelling wave solutions. The cycles of Figs. 5 and 6 occur in window II. For smaller α, there is a complex interaction of (modulated) travelling waves and heteroclinic cycles, and solutions appear to be chaotic. Even lower α gives simple spanwise travelling and modulated travelling waves. From the bifurcation diagram, it is also clear that the modes become unstable from the trivial equilibrium state in the order 2, 1, 3, 4, 5; this corresponds to the energy distribution in Fourier space, as revealed by the empirical eigenvalues (Fig. 4).

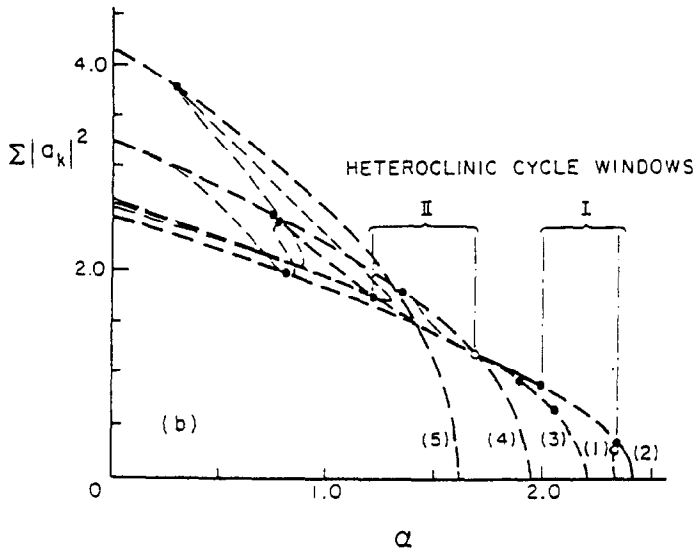

Fig. 7. Bifurcation diagram showing solutions and their stability types as α is varied. From Holmes (1990).

When the empirical eigenfunctions are derived from a different data set (for instance from a large eddy simulation of channel flow (Moin, 1984) rather than from Herzog's (1986) pipe flow experiments, which were used for the original computations of Aubry et al. (1988)) the numerical values in the bifurcation diagram change slightly, but the qualitative structure remains the same. In particular, the modes bifurcate off the trivial state in the same order, and α-ranges giving heteroclinic cycles still exist. This is encouraging confirmation that the picture of bursts and sweeps due to heteroclinic cycles is characteristic of boundary layer flows in general, and is not just a property of a particular data set or truncation.

In this respect, more realistic simulations, including nonzero streamwise modes and even a second family of empirical eigenfunctions, have been performed (Aubry and Sanghi, 1991; Sanghi and Aubry, 1993). Of course, the results are much more complicated, but they seem to embody the same "skeleton" of heteroclinic bursts found in the simpler and cruder models, while the mechanism of the bursts, in terms of the excitation of higher and streamwise modes, is captured more realistically. We also note the study of Zhou and Sirovich (1992) which overcomes the pressure boundary term problem by deriving "full-channel" eigenfunctions, weighted to emphasize wall-region dynamics, and which also includes streamwise modes.

Before briefly assessing these findings, we leave the boundary layer models to describe related work on modeling other fluid flows. We then return to our main theme to discuss symmetry in more general terms, and to present some examples in which heteroclinic cycles occur in a simpler and more transparent fashion.

8. Modeling of other open flows

The methods described above may be applied rather generally to model the dynamics of coherent structures in spatially extended systems. Indeed, the POD has been applied to mechanical vibrations,

laser dynamics, nonlinear optics, chemical processes, and even to studies of neural activity in the human brain. In fluid mechanics per se, numerous studies of closed flow systems have been done, using both experimental and numerical databases (Sirovich et al., 1989; Park and Sirovich, 1990; Sirovich and Park, 1990; Deane and Sirovich, 1991; Sirovich and Deane, 1991). Much attention has also been paid to model PDEs for weakly nonlinear waves, including the Ginzburg–Landau, Burgers, and Kuramoto–Sivashinsky equations (Sirovich and Rodriguez, 1987; Rodriguez and Sirovich, 1990; Sirovich, 1989; Chambers et al., 1988; Kirby and Armbruster, 1992; Aubry et al., 1991, 1992). In much of this work the POD is applied and its results assessed in a "static", averaged fashion. We cannot provide a proper survey of all such applications, but we do wish to place the modeling described thus far in context, by describing some other recent work on open fluid flows in which the POD was used as a basis for the derivation of low-dimensional models and some analysis of the models attempted.

We will outline five problems, the first of which is, like the boundary layer, a fully developed turbulent flow. Of the other four, two involve transition, spatial growth, and evolution of coherent structures, and two exhibit complex geometry. Both experimental and numerically generated databases are represented. These examples suggest the broad range of flows for which low-dimensional models can be made.

8.1. A circular jet

Recall Fig. 1, showing the plane mixing layer. A related example, with important technological applications, is the circular jet and its concomitant annular mixing layer. This flow has been studied by George, Glauser, and their co-workers (Glauser and George, 1987a,b; Glauser et al., 1987; Glauser et al., 1991a,b; Glauser et al., 1992; Grinstein et al., 1995; Zheng and Glauser, 1990).

The annular jet mixing layer is the region between a jet exiting from a nozzle and the ambient fluid. As in the shear layer, mixing is largely achieved by lobe-like pseudopodia: these are the coherent structures to be captured in a low-dimensional model. Circular symmetry of the jet implies homogeneity in the azimuthal direction. Radially – across the layer – the flow is clearly inhomogeneous and in the streamwise direction it is also strictly inhomogeneous, although approximate streamwise self-similarity (cf. Fig. 1) suggests that, after rescaling, one might assume homogeneity. As described below, in considering "short" subdomains, Glauser et al. did assume homogeneity, appropriate to nearly parallel flows; in other work they appealed to the Taylor hypothesis to develop a model for streamwise (spatial) evolution.

In Glauser and George (1987b) the dominant family of eigenfunctions was found to contain over 50% of the average energy, and this family of eigenfunctions alone was used in the model. The eigenvalue spectrum as a function of azimuthal (m) and streamwise (k_1) wave number is shown in Fig. 8(a). Its structure is richer than the analogous Fig. 4 for the wall layer, with peaks in the k_1-direction for $m=0$, corresponding to the jet's Strouhal (vortex-shedding) frequency, and at azimuthal mode number $m \approx 5$ for small streamwise wave number k_1 (Glauser et al., 1991b). The ridge connecting these peaks across the interior of the wave number plane indicates that any reasonable low-dimensional model should include a triangle of mixed azimuthal/streamwise modes; see Fig. 8(b).

The PDE and the boundary conditions used in the jet mixing layer study are derived in Zheng and Glauser (1990), Glauser et al. (1991b), and Grinstein et al. (1995). The equations are analogous

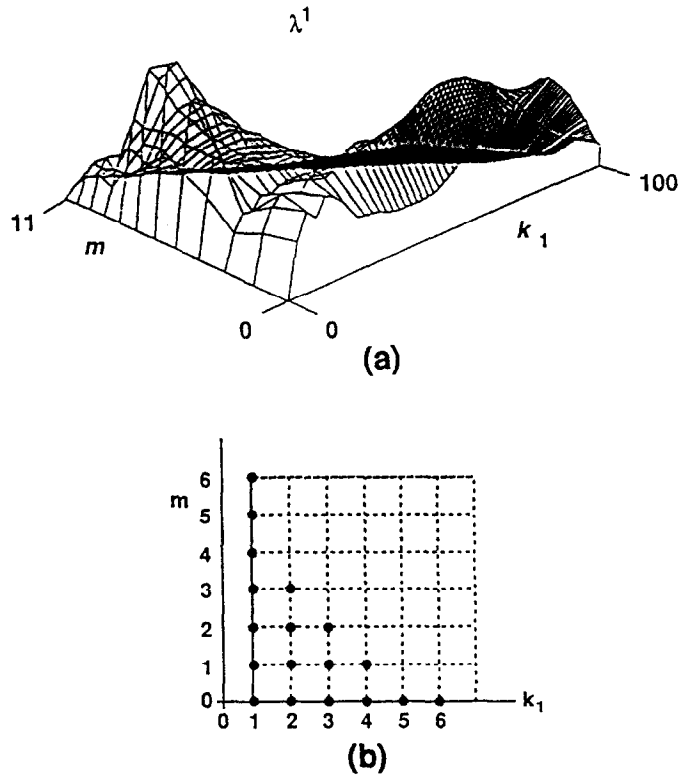

Fig. 8. (a) The spectrum of empirical eigenvalues for the dominant family in the jet study. (b) Streamwise and azimuthal wave numbers for inclusion in a dynamical model. From Glauser et al. (1991b).

to the boundary layer case of Sections 6.1–6.2, but in a cylindrical coordinate system appropriate to the jet geometry. As there, the mean velocity is related to the Reynolds stress, although there is no term corresponding to the second component of Eq. (27). A boundary condition on the pressure at the edge of the model domain was also imposed, similar to that in the boundary layer case (31), but since the domain modeled includes most of the mixing layer and fluctuating velocities are almost zero at the boundaries, the pressure terms are significantly smaller than in the wall layer model and they were neglected.

Taking a cue from the energy content revealed by the eigenvalue spectrum of Fig. 8(a), 18 (complex) modes were retained in the Galerkin projection, as indicated in Fig. 8(b), for a total of 36 real ODEs. Solutions were examined for different values of a bifurcation parameter analogous to α in the boundary layer model (33). In some parameter ranges a cascade-like phenomenon involving interaction between streamwise and azimuthal modes was seen, with net transfer of energy from modes with $m=0$, $k_1>1$ to modes with $m=4,5,6$, $k_1=1$. Reconstructed velocity fields for this parameter range show pairs of approximately azimuthally symmetric ($m=0$) vortices pairing and subsequently losing stability to $m\neq 0$ modes. Vorticity field reconstructions also suggest the creation of smaller-scale motions coincident with bursts in the modal coefficients.

Due to the imposed rotational and streamwise homogeneity, the model shares the O(2)-equivariance of the boundary layer models, and one expects to see heteroclinic cycles. Time histories and phase

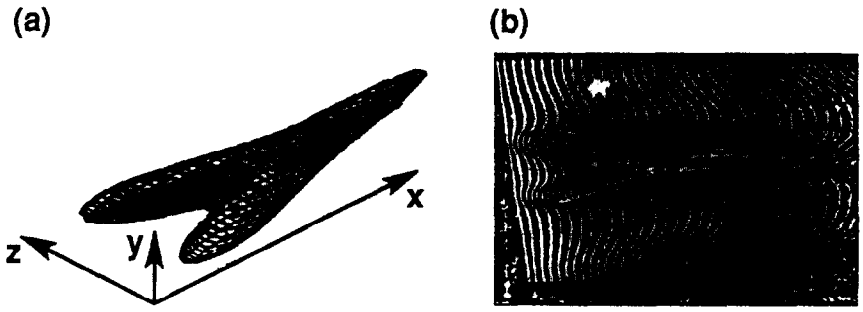

Fig. 9. Comparison of the leading eigenfunction (a) with an experimental visualization of a lambda vortex (b). From Rempfer and Fasel (1994a).

portraits of modal coefficients presented in Figs. 9–15 of Glauser et al. (1991b) suggest that such intermittent, bursting solutions do indeed occur, although detailed studies of the type described in Section 10 below remain to be done. In other parameter regions, solutions exhibit modulated travelling waves similar to those found at low loss values in the boundary layer model: see Aubry et al. (1988) and Section 7.3.

8.2. A transitional boundary layer

A second important canonical problem is the laminar to turbulent transition in a flat plate boundary layer. Rempfer and Fasel have addressed this problem in Rempfer (1993, 1994), and Rempfer and Fasel (1991, 1993, 1994a,b). Their database derives from direct numerical simulation (Rist and Fasel, 1995) of an experiment carried out earlier by Kachanov et al. (1985). The simulation enforced reflection symmetry with respect to a central, streamwise-wall normal plane, transverse to the spanwise direction, matching the (approximate) symmetry induced experimentally by use of symmetric suction and blowing. Rempfer and Fasel computed empirical eigenfunctions on several subdomains at different downstream locations within the larger computational domain.

The flow is inhomogeneous in all three directions, since it is developing in the streamwise direction and the natural spanwise translation symmetry is removed by imposition of the reflectional constraint. Two results of Rempfer and Fasel (1994a) are especially notable: first, it was shown that the POD can extract a structure similar to a lambda vortex, characteristic of transitional flows: see Fig. 9. Second (see Fig. 10) the leading empirical eigenfunctions at several streamwise locations were compared with the classical Orr–Sommerfeld eigenfunctions for a two-dimensional laminar layer, representing the streamwise velocity component of Tollmien–Schlichting waves of linear stability theory. At upstream locations, the empirical eigenfunctions are nearly identical to the Orr–Sommerfeld eigenfunctions; further downstream they differ significantly, as the weak initial instabilities evolve into more fully nonlinear forms.

In interpreting these results it is important to recognize that the leading eigenfunctions occur approximately in pairs, with almost equal eigenvalues. As we saw in Section 4.3, if the layer were perfectly translation invariant in the streamwise direction, Fourier modes would result, each of which can be expressed as real sine and cosine components associated with each double eigenvalue. The empirical functions presented in Fig. 2 of Rempfer and Fasel (1994a) are remarkably similar to these,

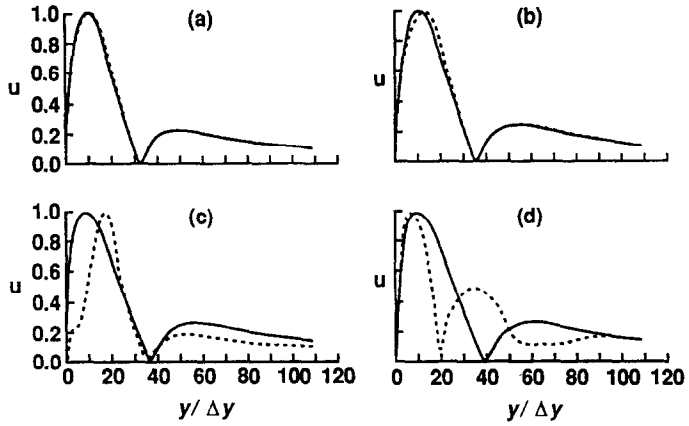

Fig. 10. Comparison of streamwise velocity profiles of the leading pair of empirical eigenfunctions with Orr–Sommerfeld eigenfunctions: (——) O–S eigenfunction; (- - - -) r.m.s. profile of empirical eigenfunction. Panels (a)–(d) represent successive downstream locations. From Rempfer and Fasel (1994a).

indicating approximate invariance in each subdomain, consistent with slowly developing structures. The coherent structures of Figs. 9 and 10 were therefore constructed as sums of corresponding pairs of eigenfunctions multiplied by the appropriate modal coefficients.

In the dynamical analyses of Rempfer (1993, 1994) the Navier–Stokes equations were projected on spaces spanned by 30–40 modes with essentially no modeling other than of energy losses to neglected modes. At the wall, the eigenfunctions satisfy the no-slip condition, while the exponential decay at the free-stream side, employed in the simulations of Rist and Fasel (1995), results in no additional boundary terms: unlike the wall-layer model, the domain encompasses essentially the whole thickness of the developing layer. Periodic boundary conditions, consistent with the symmetry constraint, were imposed in the spanwise direction. Inflow and outflow influences at the boundaries of each subdomain were not specifically modeled; essentially one appeals to the fact that the correct *combinations* of empirical eigenfunctions satisfy appropriate velocity boundary conditions on average. Energy losses to neglected modes were modeled by an effective (Heisenberg) viscosity which increases with wave number. It was not necessary to model the "quasilocal" mean velocity profile as in Section 6.1, so that the ODEs are quadratic, like the original Navier–Stokes equations.

The resulting low-dimensional models are capable of excellent short-time tracking of projections of the full direct numerical simulation (DNS) solution, as shown in Rempfer (1993), Fig. 1(a); see also Rempfer and Fasel (1994b), Fig. 2, reproduced here as Fig. 11. They also display the increasing complexity of the time-dependent modal coefficients, as one moves to subdomains further downstream and the Tollmien–Schlichting waves develop secondary instabilities. However, little is known about the geometric structure of the models in phase space, although Rempfer (1994) identifies an analogy between the equations for coherent structures and those of nonlinearly coupled multi-degree-of-freedom oscillators.

In Rempfer and Fasel (1994b) energy equations were derived for the coherent structures and energy transfer analysed. Rather than integrating model equations for the coefficients as in Rempfer (1993), the modal coefficients were obtained by projection of DNS solutions onto the appropriate

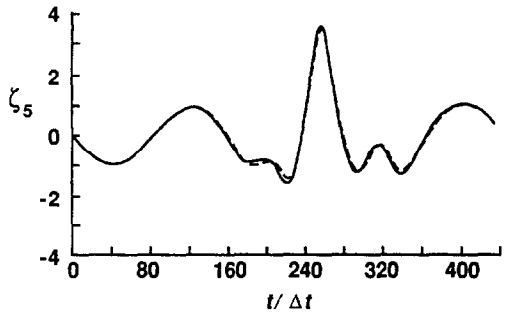

Fig. 11. Comparison of modal amplitudes of DNS and low-dimensional model data for the boundary layer: (- - - -) direct numerical simulation; (——) model. From Rempfer and Fasel (1994b).

empirical eigenfunctions. Both instantaneous and time-averaged energy flows were studied in projections comprising 34 eigenfunctions, and conclusions were drawn regarding both the energy budget which maintains the mixture of coherent structures in the fluctuating velocity field, and mechanisms involving higher-order structures in the characteristic spike events of transition.

This work differs in several respects from that on the turbulent boundary layer described above. In the latter, the assumption of spanwise and streamwise homogeneity leads to a Fourier decomposition in both these directions. Thus the experimentally observed *individual* coherent structures do not appear as single eigenfunctions, or even simple pairwise combinations, per se. Rather, various Fourier components, weighted by the solutions of the low-dimensional models, dynamically mix to produce the quasisteady rolls, streaks, and bursts displayed in Fig. 6. In contrast, here a combined pair of eigenfunctions associated with a near-multiple empirical eigenvalue derived by Rempfer and Fasel (1994a) captures much of the lambda vortex structure surprisingly well, as indicated in Fig. 9. This derives from the enforced reflection symmetry in the spanwise direction, inherited from the DNS database, which restricts consideration to a subspace of reflection-symmetric eigenfunctions. This constraint rules out propagating waves in the spanwise direction and may not permit all the physically relevant unstable modes to emerge. If such a constraint were imposed on the five-mode model of Section 7, for example, it would restrict solutions to the real subspace and would therefore preclude the exploration of heteroclinic cycles. (As described in Section 10.1 below, of the two steady heteroclinically connected solutions contained in the real subspace, one is a saddle and one a sink. Solutions restricted to this subspace would therefore die in the sink.)

8.3. A forced transitional mixing layer

Just as one may promote particular disturbances in a transitional boundary layer, other developing flows can be "locked" to applied excitations. The next example involves an acoustically excited plane mixing layer studied by Rajaee et al. (1994) (cf. Rajaee and Karlson, 1990, 1992). The database derives from experimental hot wire measurements of two-dimensional (streamwise and cross layer) velocities.

The layer was excited by a loudspeaker below a spanwise slot in the floor of the test section, with which two superposed sine waves were applied, at the unstable natural frequency and its first subharmonic frequency, separated by a (controllable) phase shift. A 270° phase difference was chosen,

having been found to suppress the development of three-dimensional motions. Two-point correlation tensors were constructed from single-point measurements by appeal to phase locking. The streamwise extent being relatively large, the flow was treated as inhomogeneous in both streamwise and cross-stream directions, and a two-dimensional POD analysis was carried out via the method of snapshots (Sirovich, 1987). The first four modes were found to capture 86% of the energy on average; the first eight contained 96%, and modes nine to 16 contributed only 1.3%. The first two modes correspond to the subharmonic and the next two modes to the natural frequency. Projections of experimental data onto these pairs of eigenfunctions reveal almost perfect sinusoidal oscillations (Rajaee et al., 1994, Fig. 6; also see Fig. 12, below). The eigenvalues within each pair are approximately equal; as in the work of Rempfer and Fasel, this reveals *approximate* streamwise homogeneity.

As in Section 6.1, the velocity field was (Reynolds) decomposed into steady and fluctuating components and a PDE written for the latter, with the time-averaged stress term modeled as a sum of empirical eigenvalues by appeal to uncorrelatedness of their expansion coefficients (10). The mean flow was treated as constant in time and viscosity was neglected as it is dynamically unimportant in this (non-turbulent) problem. As in the transition layer study above, the pressure term at the boundary of the domain of integration was set to zero. The resulting dynamical systems appear to have no particular symmetry structure in phase space.

Simulations of models containing eight and sixteen (real) modes were compared to experimental data, via projections of the latter onto individual eigenfunctions. Fig. 12 shows a sample of the results for the first eight modes of the 16 mode system. For both models, the first two modes display remarkably good tracking of the experimental time evolution, while higher modes are less faithful, although their general level remains correct for the 16 mode problem. In the eight mode system, the fifth and sixth modes exhibit growing magnitudes significantly above the experimental data. Evidently, an energy transfer mechanism, which would normally feed the ninth and higher modes, is absent in the eight mode truncation. (Such transfer could be modeled by an effective viscosity as in the boundary layer studies.)

The dynamical behavior of these models is considerably less complex than that of the transitional boundary layer models of Section 8.2. Like the experimental system, they primarily exhibit advected vortices, although there is strong evidence of vortex pairing in some snapshots (Rajaee et al., 1994, Fig. 3). The two-dimensional nature of the model may explain why solutions, without the addition of feedback or effective viscosity, do not blow up (cf. Sections 6.2 and 6.3): there is no three-dimensional vortex stretching to transfer energy into fluctuations from the mean flow. However, only relatively short integration times were presented, and long-term behavior was not considered.

8.4. Two flows in complex geometries

We have thus far viewed the POD and associated low-dimensional models as tools for the study of "canonical" flows, with a view to gaining general understanding of turbulence generation and instabilities. Can the optimality of empirical bases also help in modeling flows in complex geometries? Such flows are of great technological importance, for example, in rotating machinery. Deane and his co-workers (1991) appear to have been the first to investigate this possibility. They considered two geometries: flow in a grooved channel and in the wake of a circular cylinder. Both databases were generated by spectral element simulations, and were two-dimensional. The channel has a rectangular cavity in its bottom wall; the boundary conditions are no-slip at the walls and

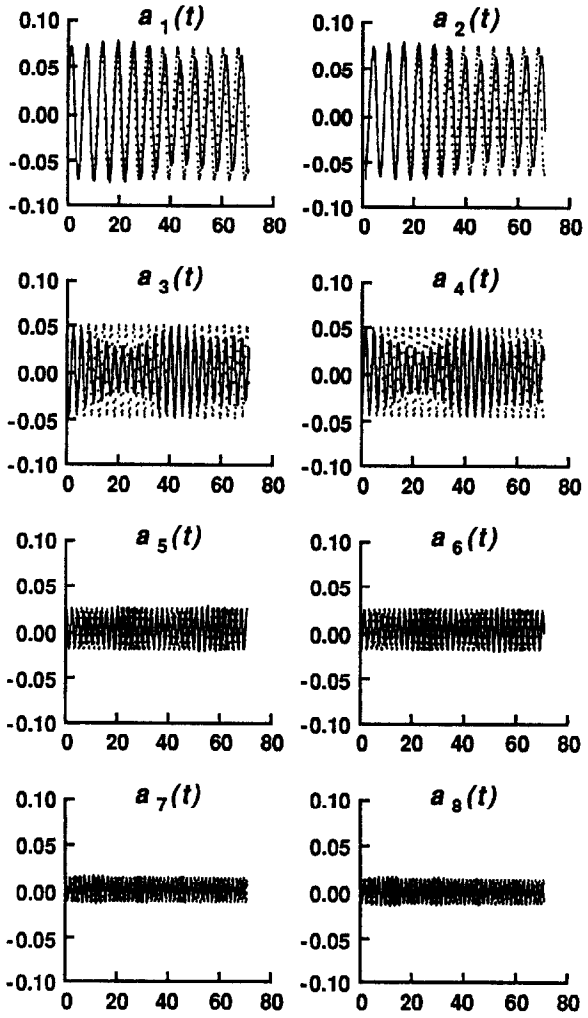

Fig. 12. Comparison of modal amplitudes of experimental and low-dimensional model data for the forced mixing layer: (- - - -) experiment; (——) 16 mode model. From Rajaee et al. (1994).

periodic in the streamwise direction, so that the domain represents one cell in a longitudinal array. The cylinder wake is dominated for a wide Reynolds number range by the Kármán street: pairs of vortices shed alternately from the upper and lower surfaces, and periodic boundary conditions are used only in the cross-stream direction. In the streamwise direction, a prescribed inflow profile and a viscous "sponge" at the outflow boundary are applied, since simple periodic conditions would allow shed vortices to re-enter the domain.

The Reynolds number for the channel flow was $Re=350$ based on 0.75 of the mean flow rate (Deane et al., 1991). (Onset of periodic oscillations was observed at $Re=300$.) In the cylinder wake, three flows were considered at Reynolds numbers of 100, 150, and 200 based on cylinder diameter. In all cases the systems exhibited limit cycles, so the temporal dynamics were, as in the

previous example, rather simple. Here the concern is primarily with spatial complexity. Superficially, the spatial form of trapped or shed vortices in problems of this type might seem highly Reynolds-number dependent, and an important question concerns the range of validity of models based on data collected at a particular Reynolds number.

Two-dimensional POD analyses were carried out, using the method of snapshots (Sirovich, 1987). Data ensembles were of modest size and restarts from different initial conditions were made, to provide an ensemble average without relying on ergodicity. In flows of this type, with simple temporal dynamics, this is clearly an important consideration. In the grooved channel flow the first two modes captured over 99% of the energy. For the cylinder wake at all three Reynolds numbers, the two leading modes captured over 97% and the first four to five modes (depending on Reynolds number) exceeded 99%. In spite of the apparent strong inhomogeneity in the streamwise direction, the leading eigenfunctions for both flows again exhibited distinct pairwise patterns and the eigenvalues occurred in approximate pairs, as in the transition and mixing layers just described.

Working in a mixed velocity/vorticity formulation, a straightforward projection of the fluctuating component of the Navier–Stokes equation was performed, with a constant mean profile. Due to the geometry and boundary conditions in both problems, and the fact that the full computational domain was included, the pressure terms vanish. In studying the performance of models for the cylinder wake over a range of Reynolds numbers, it was found that the constant-shape mean flow was the greatest single factor causing poor performance: using the corrected mean profile, even with eigenfunctions for a different Reynolds number, led to acceptable results. Similar observations applied to the grooved channel model. An empirical relation allowing for variation of mean velocity profile with Reynolds number was therefore introduced.

The authors studied dynamical systems with four modes for the grooved channel flow and observed that increasing the number of modes to eight or 16 gave comparable results. All models were based on the eigenfunctions derived from the $Re=350$ simulations. For the cylinder wake, at least six modes were necessary to obtain stable oscillations; with only four modes, oscillations appeared to grow without bound. Models were derived for Reynolds numbers of 100, 150, and 200, with the mean velocity profiles from the appropriate Reynolds number. Models using eigenfunctions from a Reynolds number of 100, with mean velocity profiles derived from higher Reynolds numbers, were also constructed.

Projections of attractors into various phase planes and bifurcation diagrams of the model ODEs were compared with those from the full simulation. A given dynamical system was found to display very good short-term tracking for the Reynolds number from which it was derived; attractor phase portraits and bifurcation diagrams also matched well. The potential for extrapolation in Reynolds number range was particularly emphasized in this work. In particular, Fig. 15 of Deane et al. (1991) is a bifurcation diagram showing the dependence of the limit cycle amplitude on Reynolds number for the cylinder wake.

This study addressed an important aspect of low-dimensional models: their capability for use at Reynolds numbers different from those for which the eigenfunctions were constructed. An early study of a model problem, the complex Ginzburg–Landau equation (Sirovich and Rodriguez, 1987; Rodriguez and Sirovich, 1990), addressed the same issue. (Note that this is not a concern for the turbulent wall-layer models of Sections 6 and 7, since those models are expressed in wall variables and so should be universal: see Section 6.3.) These results suggest that empirical eigenfunctions can significantly reduce the amount of data needed to describe and model spatially complex flows, and

that they enable one to identify at least the "pre-turbulent" bifurcations which occur in such flows. Similar ideas have been used by Noack and Eckelmann (1992, 1994a–c) to construct and analyze low-dimensional models of the cylinder wake problem.

8.5. Discussion

A number of common features emerge from the boundary layer modeling described in Sections 6 and 7 and the work summarized in the present section. In particular, low-dimensional models can reproduce the behavior of temporally simple systems, such as the forced mixing layer and low Reynolds number complex geometry flows, remarkably well. They can even display good quantitative short-time tracking capabilities, suggesting that they may be useful as models with sufficient predictive capacity for feedback control purposes, or for use in Kalman filters.

For flows of greater (spatio-) temporal complexity, such as the turbulent boundary layer and jets, one should perhaps be more modest, seeking at first only *qualitative* understanding. However, as the discussions to follow in Sections 12 and 13 indicate, we believe that these models *can* provide important information on key mechanisms such as the burst-sweep cycle. The work on the transitional boundary layer of Section 8.2, an intermediate case in complexity between the "simple" flows of Sections 8.3 and 8.4 and fully developed turbulence, supports this view. Low-dimensional models enormously simplify and significantly restrict the full behavior, but such a simplification and the identification of key features which it permits, is just what we set out to achieve.

In all cases, it seems important to include sufficiently many low-energy modes to afford reasonable energy transfer and dissipation mechanisms, or to model these as suggested in Section 6.3. Modes which are inactive on average may well undergo brief bursts of high-energy action in which they play a crucial dynamical role. Indeed, this is essentially what the odd Fourier modes do during heteroclinic cycling in the five mode model of Aubry et al. (1988): see Fig. 5.

Further general comments on the validity of low-dimensional models appear in Section 13.

9. Symmetry: translations, reflections, and O(2)-equivariance

Symmetry is a central and powerful concept in dynamics. On the one hand, it allows one to reduce the complexity, and often the dimension, of a system. On the other, symmetries have profound implications for the robustness of structures in a system under perturbation. A given solution, such as homoclinic connection, may be destroyed by the smallest general perturbation: think of the effect of weak damping on the energy-conserving saddle separatrix loop in the classical pendulum equation. However, if only perturbations consistent with the symmetries of the system are allowed (reversibility, for the pendulum), the same solution might be structurally stable and hence survive such perturbations.

We have already noted how the group O(2) appears in the boundary layer model, where it stems from translation and reflection invariance of the original physical situation (see Eqs. (34) and (35)). To appreciate better the action of O(2) on a set of Fourier modes, consider a scalar variable $w(x,t)$ expanded in a Fourier series:

$$w(x,t)=\sum_j z_j(t)\mathrm{e}^{2\pi\mathrm{i}jx/L}\,. \tag{36}$$

Translation and reflection in physical space, the x dimension, become

$$T_\alpha w(x) = w(x+\alpha) = \sum_j z_j e^{2\pi i j(x+\alpha)/L} = \sum_j (e^{2\pi i j\alpha/L} z_j) e^{2\pi i j x/L}, \tag{37}$$

$$R_f w(x) = w(-x) = \sum_j z_j e^{2\pi i j(-x)/L} = \sum_j z_{-j} e^{2\pi i j x/L}. \tag{38}$$

Remembering that in a physical system $w(x,t)$ is generally real, forcing $z_j^* = z_{-j}$, we conclude that translation and reflection in physical space induces the following actions on the coefficients of the Fourier modes:

$$T_\alpha : z_j \mapsto e^{(2\pi i j\alpha/L)} z_j, \qquad R_f : z_j \mapsto z_j^*. \tag{39}$$

T_α is a rotation in the complex plane and R_f is a reflection across the real axis. For z_1 this is precisely the standard action of O(2) on $\mathbb{C}$, the space where the coefficients live. Every member of O(2) can be constructed out of a finite combination of these transformations. The T_α's together with R_f generate O(2). For a general j, the only difference is that elements are rotated by an angle $j\alpha$, but this amounts to a simple rescaling. Thus, O(2) represents the induced action on the phase-space $\mathbb{C}^n$ by the transformations (34) and (35) for any n.

In summary, if we start with a translationally invariant system and project it onto a Fourier basis, the resulting system of ODEs for the evolution of the coefficients will exhibit O(2) symmetry. In the next section, we will take a closer look at the consequences forced by O(2) symmetry on a system, after first discussing symmetry in a broader framework.

10. Equivariant ODEs and heteroclinic cycles

Given a group of transformations Γ on a space X (e.g. $X = \mathbb{R}^n$), we say that a function $\boldsymbol{g} : X \to Y$ (where Y is some, possibly different, space, e.g. $Y = X$ or $Y = \mathbb{R}$) is Γ-invariant if

$$\boldsymbol{g}(\boldsymbol{x}) = \boldsymbol{g}(\gamma(\boldsymbol{x})) \quad \text{for all } \gamma \in \Gamma. \tag{40}$$

We call a function $\boldsymbol{f} : X \to X$ Γ-equivariant if

$$\gamma(\boldsymbol{f}(\boldsymbol{x})) = \boldsymbol{f}(\gamma(\boldsymbol{x})) \quad \text{for all } \gamma \in \Gamma. \tag{41}$$

Similarly, we call a family of ODEs

$$\dot{\boldsymbol{x}} = \boldsymbol{f}(\boldsymbol{x}) \quad \text{with } \boldsymbol{x} \in \mathbb{R}^n \tag{42}$$

Γ-equivariant if the vector field $\boldsymbol{f}$ is equivariant, i.e.

$$\gamma(\dot{\boldsymbol{x}}) = \gamma(\boldsymbol{f}(\boldsymbol{x})) = \boldsymbol{f}(\gamma(\boldsymbol{x})) \quad \text{for all } \gamma \in \Gamma. \tag{43}$$

The key implication of (43) is that, if $\hat{x}(t)$ is a particular solution of (42), then so is $\gamma\hat{x}(t)$ for any $\gamma \in \Gamma$: each solution belongs to a whole group orbit of solutions.

In general, equivariant (scalar- or vector-valued) functions are built out of "pure" equivariant elements multiplied by invariant scalar-valued functions. As an example, consider the group D_n, the group of rotation and reflection symmetries of an n-gon in the plane. Identifying the plane, $\mathbb{R}^2$, with the complex plane, $\mathbb{C}$, for notational convenience, the D_n-equivariant functions (under the standard action on $\mathbb{C}$) are of the form

$$g(z) = p(u,v)z + q(u,v)(z^*)^{n-1},$$

with $u = zz^*$ and $v = z^n + (z^*)^n$. A quick calculation shows that $(z^*)^{n-1}$ and z are equivariant and that u and v are invariant. Thus, the scalar functions $p(u,v)$ and $q(u,v)$ are invariant and the totality, $g(z)$, is equivariant.

10.1. O(2) *and normal forms*

As already noted, we are primarily interested in the implications of O(2) symmetry. In anticipation of the types of equations we will extract later, we consider a set of O(2)-equivariant ODEs of the form

$$\dot{z}_1 = f_1(z_1,z_2), \qquad \dot{z}_2 = f_2(z_1,z_2) \quad \text{with} \quad z_1,z_2 \in \mathbb{C}, \tag{44}$$

i.e. the most general form of an O(2)-equivariant ODE on $\mathbb{C}^2$. In this case the invariant functions turn out to depend only on the three combinations $|z_1|^2$, $|z_2|^2$ and $z_1^2 z_2^* + z_1^{*2} z_2$, and the equivariant vector fields are

$$\begin{pmatrix} z_1 \\ z_2 \end{pmatrix} \quad \text{and} \quad \begin{pmatrix} z_1^* z_2 \\ z_1^2 \end{pmatrix}.$$

Hence, up to third order, we have the normal form

$$\begin{aligned} \dot{z}_1 &= \mu_1 z_1 + c_{12} z_1^* z_2 + (d_{11}|z_1|^2 + d_{12}|z_2|^2) z_1, \\ \dot{z}_2 &= \mu_2 z_2 + c_{11} z_1^2 + (d_{21}|z_1|^2 + d_{22}|z_2|^2) z_2, \end{aligned} \tag{45}$$

in which all the coefficients are purely real. Assuming that $c_{12}, c_{11} \neq 0$ we can further rescale, reversing the direction of time if necessary, to obtain

$$\begin{aligned} \dot{z}_1 &= z_1^* z_2 + (\mu_1 + e_{11}|z_1|^2 + e_{12}|z_2|^2) z_1, \\ \dot{z}_2 &= \pm z_1^2 + (\mu_2 + e_{21}|z_1|^2 + e_{22}|z_2|^2) z_2, \end{aligned} \tag{46}$$

where $e_{11} = d_{11}/|c_{11}c_{12}|$, $e_{12} = d_{12}/c_{12}^2$, $e_{21} = d_{21}/|c_{11}c_{12}|$ and $e_{22} = d_{22}/c_{12}^2$. Through these rescalings, we significantly reduce the complexity, but there still remain several cases depending on the signs of the various coefficients. Here we will analyze only the case relevant to the boundary layer model in the heteroclinic cycle range presented earlier. In this case, the quadratic term in the second equation

of (46) is $-z_1^2$, and the parameters satisfy $e_{ij} < 0 < \mu_j$, and $\mu_1 - \mu_2(e_{12}/e_{22}) - \sqrt{-\mu_2/e_{22}} < 0 < \mu_1 - \mu_2(e_{12}/e_{22}) + \sqrt{-\mu_2/e_{22}}$. Then we have the following proposition:

Proposition 1. *For* $e_{ij} < 0 < \mu_j$ *and* $\mu_1 - \mu_2(e_{12}/e_{22}) - \sqrt{-\mu_2/e_{22}} < 0 < \mu_1 - \mu_2(e_{12}/e_{22}) + \sqrt{-\mu_2/e_{22}}$, *the system* (46) ("−" *case*) *has a circle of equilibria connected by heteroclinic cycles. Furthermore, if* $\mu_1 - \mu_2 e_{12}/e_{22} < 0$ *the cycles are attracting.*

Proof. First, observe that the z_2-plane, defined by $z_1 = 0$, is invariant. Seeking equilibria in this plane and remembering that $e_{ij} < 0 < \mu_j$, we find a circle (group orbit) of fixed points defined by $|z_2| = \sqrt{-\mu_2/e_{22}}$. Now let $z_j = x_j + \mathrm{i}y_j$ and consider (46) as a system on $\mathbb{R}^4$ with $(z_1, z_2) = (x_1, y_1, x_2, y_2)$. We obtain

$$\begin{aligned}
\dot{x}_1 &= x_1 x_2 + y_1 y_2 + x_1(\mu_1 + e_{11} r_1^2 + e_{12} r_2^2), \\
\dot{y}_1 &= x_1 y_2 - y_1 x_2 + y_1(\mu_1 + e_{11} r_1^2 + e_{12} r_2^2), \\
\dot{x}_2 &= -(x_1^2 - y_1^2) + x_2(\mu_2 + e_{21} r_1^2 + e_{22} r_2^2), \\
\dot{y}_2 &= -2x_1 y_1 + y_2(\mu_2 + e_{21} r_1^2 + e_{22} r_2^2),
\end{aligned} \tag{47}$$

where $r_j^2 = x_j^2 + y_j^2$. Linearizing about $(0, 0, \sqrt{-\mu_2/e_{22}}, 0)$, we get the diagonal matrix

$$\begin{bmatrix} \lambda_+ & 0 & 0 & 0 \\ 0 & \lambda_- & 0 & 0 \\ 0 & 0 & -2\mu_2 & 0 \\ 0 & 0 & 0 & 0 \end{bmatrix}, \tag{48}$$

where

$$\lambda_\pm = \mu_1 - (\mu_2 e_{12}/e_{22}) \pm \sqrt{-\mu_2/e_{22}}\,. \tag{49}$$

Because these equations are equivariant under rotation about the origin, this structure will be preserved around the circle of equilibria. In the light of our assumptions on the parameters, we have a two-dimensional stable and a one-dimensional unstable manifold emanating from each point of the circle. Furthermore, by looking at Eqs. (47), one sees that the real subspace, *span*$\{(1,0,0,0), (0,0,1,0)\}$, is invariant. For the moment, we focus on the two points where the circle of fixed points intersects this invariant plane, namely $A = (0, 0, \sqrt{-\mu_2/e_{22}}, 0)$ and $B = (0, 0, -\sqrt{-\mu_2/e_{22}}, 0)$. Looking at the equations as expressed in (47) and setting $y_1 = y_2 = 0$, we see that A is a saddle and B a sink. Orbits leaving A are trapped in a bounded disc, and since there are no equilibria or limit sets in the half spaces $\{x_1 > 0\}$ and $\{x_1 < 0\}$, they must limit on B. Thus, we have a heteroclinic orbit from A to B. By judicious application of the O(2) symmetry given by transformation (39), we can complete the picture. The application of $T_{\pi/2}$ amounts to a rotation by $\pi/2$ in the z_1 plane and by π in the z_2 plane. In coordinates, this gives

$$T_{\pi/2} : (x_1, y_1, x_2, y_2) \mapsto (y_1, -x_1, -x_2, -y_2)\,.$$

Application of $T_{\pi/2}$ permutes the connections from A to B, giving a connection from B to A living in the plane defined by $\{y_2 = x_1 = 0\}$. Thus, we establish the presence of a heteroclinic cycle containing

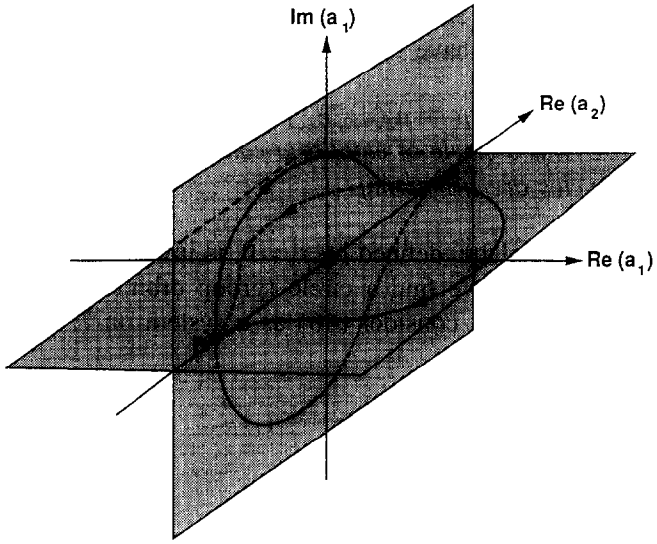

Fig. 13. A and B are connected by a pair of symmetric heteroclinic cycles.

A and B (see Fig. 13). Application of T_α for arbitrary α shows that every diametrically opposed pair of equilibria on the circle $|z_2| = \sqrt{-\mu_2/e_{22}}$ is connected in such a heteroclinic cycle.

Determining the asymptotic stability of this connection is a subtle process, and we refer the reader to Armbruster et al. (1988) for the details. It turns out that the stability is determined solely by the ratio of λ_-/λ_+: If $-\lambda_-/\lambda_+ > 1$, the heteroclinic cycle is attracting while if $-\lambda_-/\lambda_+ < 1$ it is unstable. □

It should be emphasized that the heteroclinic cycles exist for an open set of parameter values. Any perturbations which respect the O(2) symmetry will leave the equations, up to third order, in the functional form dictated by (46). Thus, a small perturbation, measured in a suitable function space, will only give rise to a small change in the coefficients and therefore leave the heteroclinic cycle intact.

As noted in Section 7.3, a similar heteroclinic cycle occurs in the 5-mode model of Aubry et al. (1988), and is responsible for the solutions shown in Fig. 5. Here the circle of equilibria lies in the (a_2, a_4) even mode subspace, intersecting the real subspace at the points $(x_1, x_2, x_3, x_4, x_5) = (0, \mp\rho_2, 0, -\rho_4, 0)$, and the unstable manifolds of each point are two-dimensional. Within the real subspace, A is a saddle and B a sink; the unstable manifold of A lies in the (x_1, x_3, x_5) subspace and a connection from A to B can easily be observed numerically, although a rigorous construction involving positively invariant regions is still lacking. Accepting this "first" connection, however, the cycle follows just as with the simpler four-dimensional case above.

With the above structures in hand, the model's "bursting" and "sweeping" behavior is understandable in terms of motions in the phase plane. As described in Section 7.3, bursting and sweeping correspond to the rapid transitions from the neighborhood of one fixed point to that of another along a trajectory shadowing a heteroclinic connection, the momentary activity of the 1, 3, 5 modes causing break-up and coalescence of the streamwise vortices. In the light of the symmetries of the problem

and the above discussion, such connections are quite natural and generic. The even modes experience a net phase shift after each circuit, reminiscent of the observed spatial displacement between successive burst/sweep events. However, there is no particular time scale associated with attracting cycles: solutions spend successively longer periods lingering near the saddle points as they approach the cycle. We address this when we consider the restoration of the pressure term, in Section 12.

11. The Kuramoto–Sivashinsky equation

We now briefly turn to an example which shares the O(2) symmetry of the boundary layer model and exhibits heteroclinic cycles, but which is considerably simpler and easier to understand than the latter, namely the one-dimensional Kuramoto–Sivashinsky (KS) equation,

$$N(u) = u_t + u_{xx} + u_{xxxx} + \tfrac{1}{2}(u_x)^2 = 0\,, \tag{50}$$

with L-periodic boundary conditions. Originally, this equation was proposed in a model for instabilities in flame fronts (Sivashinsky, 1977) and for "phase turbulence" in chemical reactions. The KS equation and related equations have been used to model various interfacial instabilities, and a multi-dimensional version has been proposed to model weak fluid turbulence (Hyman et al., 1986). We make no claim that the one-dimensional KS equation has any direct relevance to turbulence; however, there are some parallels with the NS equations. The u_{xx} term is comparable to $\boldsymbol{u}\cdot\nabla\boldsymbol{U}$, as both introduce energy into the system and consequently destabilize it. Similarly, the u_{xxxx} term, like the dissipative $-\nu\nabla^2\boldsymbol{u}$ NS term, removes energy from the system and provides a stabilizing effect. In contrast to the NS equations, however, in the KS system, we can complete our analytical program in the vicinity of low-order bifurcation points, justifying almost all of our steps rigorously.

11.1. Galerkin projection

The KS equation is invariant under translations and reflections in x. As observed in the previous section, this implies that the POD eigenbasis will simply be a Fourier basis, and that the system of ODEs resulting from projecting onto the basis will be O(2)-equivariant. Setting

$$u(x,t) = \sum_j a_j(t)\phi_j(x) = \sum_j a_j(t)\mathrm{e}^{\mathrm{i}j2\pi x/L}\,, \tag{51}$$

we perform a Galerkin projection to obtain

$$\int_0^L \left\{\sum_k \left[\dot{a}_k\phi_k - \left(\frac{2\pi k}{L}\right)^2 a_k\phi_k + \left(\frac{2\pi k}{L}\right)^4 a_k\phi_k + \frac{1}{2}\left(\frac{2\pi \mathrm{i}k}{L}a_k\phi_k\right)\sum_j\left(\frac{2\pi \mathrm{i}j}{L}a_j\phi_j\right)\right]\phi_l^*\right\}\mathrm{d}x = 0\,. \tag{52}$$

The first three terms reduce by the orthogonality property of the Fourier basis:

$$(\phi_k,\phi_l) = \int_0^L \mathrm{e}^{2\pi\mathrm{i}(k-l)x/L}\mathrm{d}x = \delta_{kl}L\,. \tag{53}$$

After some rearrangement, the last term is simplified by the same reasoning:

$$\int_0^L \phi_k \phi_j \phi_l^* \, dx = \int_0^L e^{\frac{2\pi i(k+j-l)x}{L}} \, dx = (\phi_{j+k}, \phi_l) = \delta_{(k+j)l} L \,. \tag{54}$$

Thus, we arrive at

$$\dot{a}_l - \left(\frac{2\pi l}{L}\right)^2 a_l + \left(\frac{2\pi l}{L}\right)^4 a_l - \frac{1}{2}\left(\frac{2\pi}{L}\right)^2 \sum_j j(l-j) a_j a_{l-j} = 0 \,. \tag{55}$$

By dividing through by $(2\pi/L)^2$ and rescaling time by the same factor we can obtain the following slightly less cluttered equations for the a_j's:

$$\dot{a}_l = l^2 \left(1 - \left(\frac{2\pi l}{L}\right)^2\right) a_l + \frac{1}{2} \sum_j j(l-j) a_j a_{l-j} \,. \tag{56}$$

This relation applies to the truncation at any order. If we keep terms to up order K, then Eq. (56) defines an ODE on a $(2K+1)$-dimensional complex space. This can be reduced to a $2K$-dimensional complex space by noting that the evolution of the zeroth mode, a_0, is determined by the other modes:

$$\dot{a}_0 = -\frac{1}{2} \sum_{j=-K}^{K} j^2 a_j a_{-j} = -\frac{1}{2} \sum_{j=-K}^{K} j^2 a_j a_j^* = -\sum_{j=1}^{K} j^2 |a_j|^2 \,. \tag{57}$$

In (57) we have used the fact that u is real, which implies $a_j = a_{-j}^*$. The reality of u in fact means that we need consider only half of the remaining coefficients in our dynamical system (56), those with positive l. Hence, (56) effectively becomes a K-dimensional system of complex ODEs (or a $2K$-dimensional system if viewed as real ODEs).

Note that Eq. (56) is equivariant under the group O(2) with the representation (39), regardless of how many modes are included. Furthermore, the structure of (56) is identical to that of the linear and quadratic terms in the particular $K_1=0$, $N=1$ case of the boundary layer model in (33).

11.2. Bifurcation and center manifold reduction

Treating L as a bifurcation parameter, a linear stability analysis of the origin $u=0$ (i.e. $a_l=0$ for all $l \in \mathbb{Z}$) reveals that there is a series of bifurcations from the origin. Specifically, the linearization

$$\dot{a}_l = l^2 \left(1 - \left(\frac{2\pi l}{L}\right)^2\right) a_l \tag{58}$$

implies that a pair of eigenvalues passes through zero when $L=2\pi n$ for each $n \in \mathbb{N}$. Therefore at $L=2\pi n$, we have a two (real)-dimensional center manifold, a $2(n-1)$ (real)-dimensional unstable manifold and an infinite dimensional stable manifold consisting of all of the higher-order modes. The double eigenvalue is characteristic of O(2)-equivariance. If we are interested in the behavior of our model around one of these bifurcations points, it is reasonable to use a model including the center and unstable dimensions and to appeal to a center-unstable manifold reduction to include information about the stable directions. Armbruster et al. (1989), from whom this discussion is adapted, performed such a reduction.

For example, for $L \approx 4\pi$ we have a real two-dimensional unstable space and a two-dimensional center space spanned by a_1 and a_2, respectively. Of course, Eq. (56) implies that these variables are coupled to all of the remaining a_j's. Rather than simply truncate the system we choose to use a center manifold reduction (Guckenheimer and Holmes, 1983) to obtain analytic approximations for "stable" coordinates in terms of the center and unstable directions, locally near $L = 4\pi$. As usual, these are expressed as power series in the center manifold coordinates. Substituting back into the equations and truncating at cubic order we obtain

$$\begin{aligned} \dot{a}_1 &= (\tfrac{3}{4} + \mu)a_1 - 2a_1^* a_2 - a_1|a_2|^2 , \\ \dot{a}_2 &= 16\mu a_2 + \tfrac{1}{2}a_1^2 - a_2(\tfrac{1}{2}|a_1|^2 + \tfrac{1}{3}|a_2|^2) . \end{aligned} \tag{59}$$

Notice that this is a specific example of the O(2) normal form encountered previously. As explained at the onset, this was expected because of the translation invariance in physical space. However, it should be noted that we would not have obtained the cubic terms had we simply truncated the Fourier series expansion. They play a role (and have a form) similar to that of the "feedback" term introduced in modeling the mean flow $U(x_2, t)$ in the boundary layer model, but here their origin is mathematically clear: they derive from the center manifold reduction and no "physical" order of magnitude arguments are required.

Analysis of the dynamics and bifurcations of reduced models such as (59), and of models including higher-order effects, may be found in Armbruster et al. (1989).

12. Perturbed heteroclinic cycles, timing and experimental observations

Thus far, our analysis of the boundary layer model has explained how it correctly mimics the experimentally observed bursting and sweeping events and seems to capture the fact that sequential burst/sweep events tend to be spatially displaced relative to one another. However, attracting heteroclinic cycles do not possess a distinct time scale; as noted at the end of Section 10, they "die out". In reality, bursting events are observed to be sprinkled randomly in time about a mean rate, with distributions having fairly pronounced exponential tails (Holmes and Stone, 1992).

Up to this point in our analysis, we have ignored the effect of the pressure term, $\xi(t)$, arising from the free boundary conditions at the top of the boundary layer. As mentioned in Section 6.5, direct numerical simulations suggest that this term is typically two orders of magnitude smaller than the a_i's. For the majority of the phase space, this amounts to a negligible perturbation. However, in the neighborhood of a saddle point, the a_i's are considerably smaller in magnitude than in the rest of the flow and the effect of $\xi(t)$ is no longer negligible. We will now show that restoration of the pressure term $\xi(t)$ in (33), modeled by Gaussian white noise, can reproduce a well-defined characteristic time scale and exponential distributions of bursting events through its influence on the dynamics in the neighborhood of the heteroclinic cycle.

Though simulations show $\xi(t)$ to be correlated on short time scales and across (spanwise) Fourier wave numbers, as a first approximation we will take $\xi(t)$ to be standard i.i.d. white noise which is uncorrelated in time. (We note that the effect of the pressure term appears insensitive to the particular white noise form of the forcing discussed here; Stone and Holmes (1989), using a time series for $\xi(t)$ obtained from numerical data of Moin, found qualitatively similar results.) We will briefly discuss

the behavior of trajectories in the vicinity of a saddle point when white noise is included. Before we do, however, it is instructive to note that this is the first point at which we have turned to random perturbations to explain the system's behavior. In particular, the pulsing burst/sweep behavior seems intrinsic to the flow in the boundary layer and is not driven by perturbations from other regions of the flow, only perhaps triggered by them.

12.1. The noisy connection

As a model for the effect of noise on a heteroclinic cycle, we consider a single saddle point connected to itself in a homoclinic loop; for extension to heteroclinic cycles we merely combine the effects of several such saddles. In a sufficiently small neighborhood U_δ of such a saddle point, the flow is well approximated by its linearization about the fixed point. Consequently in U_δ, we model the flow by

$$dx_1 = \lambda_s x_1 dt + \varepsilon\, dW_1(t)\,, \qquad dx_2 = \lambda_u x_2 dt + \varepsilon\, dW_2(t)\,, \tag{60}$$

where dW_i is the formal derivative of a standard Brownian motion $W_i(t)$. This is an example of the well-studied Ornstein–Uhlenbeck (OU) process; see Arnold (1974). Outside U_δ, we neglect the random perturbations, supposing that during the bounded time interval needed to traverse the rest of the heteroclinic connection the relatively large deterministic part of the flow dominates. To simplify the analysis further, we also ignore the finite distortion which a distribution of solutions would experience between the time it leaves U_δ along the unstable eigenspace and when it re-enters along the stable eigenspace. Detailed analysis of this system can be found in Stone and Holmes (1990); we only sketch the main results in the context of the boundary layer model.

Solving the Kolmogorov–Fokker–Planck equation for the one-dimensional OU process, one finds the equilibrium probability density, conditioned on being at x_0 at $t=0$, to be that of a mean zero Gaussian distribution, namely

$$p(x,t\,|\,x(0)=x_0) = \mathcal{N}(x_0 e^{\lambda t}, (\varepsilon^2/2\lambda)(e^{2\lambda t}-1))\,. \tag{61}$$

Our model is built of two uncoupled OU processes: one stable and one unstable, corresponding to $\lambda_s<0$ and $\lambda_u>0$, respectively. We are interested in the competition between the two effects. We begin by assuming $-\lambda_s>\lambda_u>0$ to match the situation in the boundary layer model (attracting cycles). Analysis shows that even with the noise, $\langle x_j\rangle \to 0$ as $t\to\infty$: the stable direction still wins. But how are the passage times through U_δ affected by the noise terms? Since we neglect any distortion outside U_δ, we need only study how a Gaussian distribution with mean zero will evolve in the unstable direction when injected to U_δ along the stable direction. From (61), we see that the stable OU process possesses $\mathcal{N}(0,-\varepsilon^2/2\lambda_s)$ as a limiting distribution. Thus, we assume that the solution "particle packet" has this distribution when entering along the stable direction. It will then be ejected in the unstable direction and evolve according to

$$p\left(x,t\,\middle|\,\mathcal{N}\left(0,-\frac{\varepsilon^2}{2\lambda_s}\right)\right) = \mathcal{N}\left(0,-\frac{\varepsilon^2}{2\lambda_s}e^{2\lambda_u t}+\frac{\varepsilon^2}{2\lambda_u}(e^{2\lambda_u t}-1)\right)\,. \tag{62}$$

This can be seen by thinking of the initial Gaussian profile as having evolved from a delta density existing at time $t'<0$ such that it achieves the distribution $\mathcal{N}(0,-\varepsilon^2/2\lambda_s)$ at $t=0$. Thus, the result

of the Gaussian distribution evolved for a time t is the same as that of a delta distribution evolved for a time $\tau = t + |t'|$. More explicitly,

$$p\left(x,t\left|\mathcal{N}\left(0,-\frac{\varepsilon^2}{2\lambda_s}\right)\right.\right) = p(x,t\,|\,x(t') = x(t-\tau) = 0) = p(x,\tau\,|\,x(0) = 0)$$

$$= \mathcal{N}\left(0,\frac{\varepsilon^2}{2\lambda_u}(e^{2\lambda_u\tau}-1)\right), \qquad \tau = t + \frac{1}{2\lambda_u}\ln\left(1-\frac{\lambda_u}{\lambda_s}\right) .$$

The probability that the solution leaves the interval $[-\delta,\delta]$ in the unstable direction at or before time s is

$$P_{\text{escape}}(s) = 1 - \int_{-\delta}^{\delta} p(x_2,s\,|\,x_2 = 0)\,dx_2 \ ; \tag{63}$$

from this, the mean passage time can be estimated. In the limit where $\varepsilon \ll \delta$, it can be shown that

$$\text{Expected}(T_{\text{total}}) = K_1 + \frac{1}{\lambda_u}\{\ln(1/\varepsilon) + K_2\} \ , \tag{64}$$

where T_{total} is the overall circuit time around the cycle; see Holmes et al. (1996). Here K_1 and K_2 are constants which depend on the global structure of the heteroclinic connection and the size of U_δ, but are independent of the magnitude of the noise, ε. K_1 is basically the time required for global passage on the cycle outside U_δ (the burst/sweep) while K_2 is related to the local dynamics linearized at the saddle point (inside U_δ). For $\varepsilon = 0$ the expected escape time is unbounded, corresponding to the attracting cycle which "dies out". Introduction of the noise term reduces the expected escape time as $\ln(1/\varepsilon)$ at leading order, thereby providing a characteristic interburst time scale in our model. Furthermore, this analysis predicts a distribution of escape times with exponential tails. Stone and Holmes (1989, 1990) have confirmed these asymptotics in numerical simulations.

12.2. Noise and the boundary layer

In the boundary layer, the time interval for which a trajectory is trapped in the neighborhood of the fixed point corresponds to the time elapsing between sweep/burst events in the local domain of the model. In fact, there is considerable evidence for exponential tails from experimental data. However, once the timescales of Aubry et al. (1988) are corrected as noted in Section 7.1, the "raw" bursting rates obtained from (64) with suitable estimates for ε (the r.m.s. pressure field) are still substantially lower than those observed experimentally. Noting additionally that direct numerical simulations on the minimal flow unit of Jiménez and Moin (1991), similarly sized in $L_1 \times L_3$, also yields much slower cyclic behavior than that observed, we now believe that this is due to the spatially localized model's retention of only a single structure in the streamwise direction.

In reality, a succession of quasi-independent structures each of typical streamwise extent L_1 is swept past a stationary sensor, at a velocity U characteristic of the wall-normal location of the sensor. Thus, structures are sampled at a mean rate U/L_1 with the expected interburst duration being obtained by averaging over the probability of n structures passing in succession, none of which are bursting. Identifying $T_o = K_1$ in (64) with the duration of a burst/sweep event and $T_i = (1/\lambda_u)\{\ln(\frac{1}{\varepsilon}) + K_2\}$ with the expected interburst duration for a single structure, the probability of passage of n "quiet"

structures is $(1-p)^n$, where $p = T_o/(T_o + T_i)$ is the probability that a structure is bursting. This leads to an estimate of observed bursting rate at a fixed sensor of

$$\text{Expected}(T_{\text{burst}}) = \frac{L_1}{U} \cdot \frac{1}{p} = \frac{L_1}{U}\left[1 + \frac{1}{\lambda_u K_1}\left\{\ln\left(\frac{1}{\varepsilon}\right) + K_2\right\}\right], \tag{65}$$

in terms of the quantities in (64). Insertion of physically reasonable estimates for L_1 and U in (65) yields bursting rates within the range of experimental observation. See Podvin et al. (1997) or Holmes et al. (1996) for details and further discussion of this timing issue.

It must also be said that experimental and numerical data shows that the pressure is far from a delta correlated white noise process (see Stone and Holmes (1989) for remarks and analysis of numerical simulations). Nonetheless, the analysis suggests how quasi-random fluctuations might give rise to a distribution of passage times consistent with what is observed.

13. Conclusion

In the space of this article, we have only been able to sketch some of the mathematical and physical elements which form the basis of a model for the dynamics of coherent structures, in particular in boundary layer turbulence. A more comprehensive and critical discussion is found in the book by Holmes et al. (1996). We emphasize that the modeling process described here can yield at best a crude model, or cartoon, of the intricate processes occurring in turbulence generation in general, and the boundary layer in particular. Much physics must inevitably be averaged out, modeled, lost in the low-dimensional truncation or simply ignored. In order to obtain reasonably tractable, low-dimensional models, we pay the price of only capturing the behavior of the most energetic coherent structures; moreover, we model only a localized spatial domain of spanwise and streamwise extent comparable to that of an individual burst/sweep event, and thus artificially "extract" a single representative from a stream of evolving and interacting coherent structures.

Nevertheless, in spite of these simplifications and approximations, the models described here *do* seem to create a basis for understanding the dynamics of such structures. Through the technique of proper orthogonal decomposition, we are able to identify the most energetic modes, onto which we project the governing equations by the Galerkin method, together with modeling of neglected modes and boundary conditions, to obtain a reasonably tractable low-dimensional dynamical system. Numerical simulation, combined with analysis of the symmetries of the system and of simpler, related equations, enables us to gain some understanding of the system behavior.

In particular, the presence of stable heteroclinic cycles may be established, which appears to account for the observed burst/sweep behavior in the boundary layer. The inclusion of random noise, to model the influence of the pressure at the outer boundary of the wall region, yields a prediction of an exponential distribution of interburst intervals. This agrees qualitatively with what is detected experimentally. Numerical investigations of systems including substantially more modes, in less violent truncations, give results generally consistent with these observations.

The identification of burst-sweep dynamics with a heteroclinic attractor in a spatially localised model almost certainly simplifies the complex events occurring in the boundary layer, but we believe that the cycle identified in the low-dimensional models does provide a skeleton to which muscles and flesh will ultimately be added by models which include more modes. The work of Aubry and

Sanghi (1991), Sanghi and Aubry (1993) and of Zhou and Sirovich (1992) are steps in this direction. A more realistic picture yet, might include a "sea" of such models, loosely coupled in space, leading to a quasirandom space–time array of bursts and sweeps, as is actually observed. Such a model would also presumably provide better quantitative agreement with experimental observations of phenomena such as burst-sweep durations (see Section 12.2).

This notion of a weakly coupled sea may be practically useful. It implies that one may be able to make local modifications to an open flow, based only on local information, to achieve local turbulence control, without having the full flow field (system state) in hand. Such an effort for the boundary layer has begun. Coller et al. (1994a–c; Coller and Holmes, 1997) address mathematical and control-theoretic issues relevant to stabilizing heteroclinic cycles in the presence of noise. In these papers, motivated by the idea that controlled streamwise vorticity can be added in the wall region by suction and blowing, or by micro-mechanical actuators – see Bandyopadhyay (1994) – models of the type discussed in Sections 6, 7 and 10 are considered. Controlled vorticity, expressed as a cross-stream velocity profile (Coller et al., 1994b), adds rotational terms to the ODEs which permit one to steer incoming solutions closer to the unstable saddle points in the cycle and hence to delay bursting; cf. Ott et al. (1990).

In sum, the present approach to low-dimensional modeling of turbulence forms the foundation for a new approach to the understanding of the dynamics of coherent structures in certain turbulent flows.

Acknowledgements

This review is an expanded version of notes prepared by JCM and RWW from lectures given at the Newton Institute, Cambridge, UK, in August 1995 by PJH, to appear in the NATO/ASI proceedings of the workshop "From Finite to Infinite Dimensional Dynamical Systems". The research described here was supported in part by Contract No. F49620-92-J-0287 jointly funded by the US Air Force Office of Scientific Research (Control and Aerospace Programs) and the US Office of Naval Research; in part by Grant No. F49620-92-J-0038, funded by the US Air Force Office of Scientific Research (Aerospace Program); in part by the Physical Oceanography Programs of the US National Science Foundation (Contract No. OCE-901 7882) and the US Office of Naval Research (Grant No. N00014-92-J-1547); and in part by the Department of Energy (Grant No. DE-FG02-95ER25238).

References

Armbruster, D., Guckenheimer, J., Holmes, P., 1988. Heteroclinic cycles and modulated travelling waves in systems with O(2) symmetry. Physica D 29, 257–282.

Armbruster, D., Guckenheimer, J., Holmes, P., 1989. Kuramoto-Sivashinsky dynamics on the center unstable manifold. SIAM J. Appl. Math. 49, 676–691.

Armbruster, D., Heiland, R., Kostelich, E.J., 1994. KLTOOL: a tool to analyze spatio-temporal complexity. Chaos 4 (2), 421–424.

Arnold, L., 1974. Stochastic Differential Equations. Wiley, New York.

Aubry, N., Guyonnet, R., Lima, R., 1991. Spatio-temporal analysis of complex signals: theory and applications. J. Stat. Phys. 64 (3/4), 683–739.

Aubry, N., Guyonnet, R., Lima, R., 1992. Spatio-temporal symmetries and bifurcations via bi-orthogonal decompositions. J. Nonlinear Sci. 2, 183–215.

Aubry, N., Holmes, P., Lumley, J.L., Stone, E., 1988. The dynamics of coherent structures in the wall region of a turbulent boundary layer, J. Fluid Mech. 192, 115–173.

Aubry, N., Sanghi, S., 1991. Bifurcations and bursting of streaks in the turbulent wall layer, In: Lesieur, M., Métais, O. (Eds.), Turbulence and Coherent Structures. Kluwer, Dordrecht, pp. 227–251.

Bandyopadhyay, P.R. (Ed.) 1994. Application of Microfabrication to Fluid Mechanics, Vol. FED-197. Amer. Soc. Mech. Eng., New York.

Berkooz, G., 1991. Turbulence, coherent structures, and low dimensional models. Ph.D. thesis, Cornell University.

Berkooz, G., 1994. An observation on probability density equations, or, when do simulations reproduce statistics? Nonlinearity 7, 313–328.

Berkooz, G., Holmes, P., Lumley, J.L., 1993. The proper orthogonal decomposition in the analysis of turbulent flows. Ann. Rev. Fluid Mech. 25, 539–575.

Berkooz, G., Holmes, P., Lumley, J.L., 1993b. On the relation between low-dimensional models and the dynamics of coherent structures in the turbulent wall layer. Theoret. Comput. Fluid Dyn. 4, 255–269.

Brown, G.L., Roshko, A., 1974. On density effects and large structure in turbulent mixing layers. J. Fluid Mech. 64, 775–816.

Cantwell, B., 1990. Future directions in turbulence research and the role of organized motion. in: Lumley J.L. (Ed.), Whither Turbulence? Turbulence at the Crossroads. Springer, Berlin, pp. 97–131.

Chambers, D.H., Adrian, R.J., Moin, P., Stewart, D.S., Sung, H.J., 1988. Karhunen–Loève expansion of Burgers model of turbulence. Phys. Fluids 31, 2573–2582.

Coller, B.D., Holmes, P., 1997. Suppression of bursting. Automatica 33, 1–11.

Coller, B.D., Holmes, P., Lumley, J.L., 1994a. Controlling noisy heteroclinic cycles. Physica D 72, 135–160.

Coller, B.D., Holmes, P., Lumley, J.L., 1994b. Interaction of adjacent bursts in the wall region. Phys. Fluids 6 (2), 954–961.

Coller, B.D., Holmes, P., Lumley, J.L., 1994c. Control of bursting in boundary layer models. Appl. Mech. Rev. 47 (6), part 2, S139–S143.

Deane, A.E., Kevrekidis, I.G., Karniadakis, G.E., Orszag, S.A., 1991. Low-dimensional models for complex flows: application to grooved channels and circular cylinders. Phys. Fluids A 3 (10), 2337–2354.

Deane, A.E., Sirovich, L., 1991. A computational study of Rayleigh–Bénard convection. Part I. Rayleigh number scaling. J. Fluid Mech. 222, 231–250.

Doering, C.R., Gibbon, J.D., 1995. Applied Analysis of the Navier–Stokes Equations. Cambridge University Press, Cambridge, UK.

Foias, C., Temam, R., 1989. Gevrey class regularity for the solutions of the Navier–Stokes equations. J. Funct. Anal. 87, 359–369.

Glauser, M.N., George, W.K., 1987a. Orthogonal decomposition of the axisymmetric jet mixing layer including azimuthal dependence. In: Comte-Bellot, G., Mathieu, J. (Ed.), Advances in Turbulence. Springer, New York, pp. 357–366.

Glauser, M.N., George, W.K., 1987b. An orthogonal decomposition of the axisymmetric jet mixing layer utilizing cross-wire velocity measurements. In: Proc. 6th Symp. on Turbulent Shear Flows. Ecole Nationale Superieure de l'Aeronautique et de l'Espace and ONERA Centre d'Etudes et de Recherches de Toulouse, Toulouse, France, pp. 10.1.1–10.1.6.

Glauser, M.N., Leib, S.J., George, W.K., 1987. Coherent structures in the axisymmetric turbulent jet mixing layer. In: Durst, F., Launder, B.E., Lumley, J.L., Schmidt, F.W., Whitelaw, J.H. (Eds.), Turbulent Shear Flows 5. Springer, New York, pp. 134–145.

Glauser, M.N., Zheng, X., Doering, C.R., 1991a. The dynamics of organized structures in the axisymmetric jet mixing layer. In: Lesieur, M., Métais, O. (Eds.), Turbulence and Coherent Structures. Kluwer, Dordrecht, pp. 253–265.

Glauser, M.N., Zheng, X., Doering, C.R., 1991b. A low-dimensional dynamical systems description of the axisymmetric jet mixing layer. Technical Report MAE-247, Clarkson University.

Glauser, M.N., Zheng, X., George, W.K., 1992. The streamwise evolution of coherent structures in the axisymmetric jet mixing layer. In: Gatski, T.B., Sarkar, S., Speziale, C.G. (Eds.), Studies in Turbulence. Springer, New York, pp. 207–222.

Grinstein, F.F., Glauser, M.N., George, W.K., 1995. A low-dimensional dynamical systems description of coherent structures in the axisymmetric jet mixing layer. In: Green, S.I. (Ed.), Fluid Vortices. Kluwer, Dordrecht, pp. 65–94.

Guckenheimer, J., Holmes, P., 1983. Nonlinear Oscillations, Dynamical Systems and Bifurcations of Vector Fields. Springer, New York.

Herzog, S., 1986. The large scale structure in the near wall region of a turbulent pipe flow. Ph.D. Thesis, Cornell University.

Holmes, P., 1990. Can dynamical systems approach turbulence? In: Lumley, J.L. (Ed.), Whither Turbulence? Turbulence at the Crossroads. Springer, Berlin, pp. 195–249.

Holmes, P., Lumley, J.L., Berkooz, G., 1996. Turbulence, Coherent Structures, Dynamical Systems and Symmetry. Cambridge University Press, Cambridge, UK.

Holmes, P., Stone, E., 1992. Heteroclinic cycles, exponential tails and intermittency in turbulence production. In: Gatski, T.B., Sarkar, S., Speziale, C.G. (Eds.), Studies in Turbulence, Springer, New York, pp. 179–189.

Hopf, E., 1948. A mathematical example displaying the features of turbulence. Comm. Pure Appl. Math. 1, 303–322.

Hyman, J.M., Nicolaenko, B., Zaleski, S., 1986. Order and complexity in the Kuramoto-Sivashinsky model of weakly turbulent interfaces. Physica D 23, 265–292.

Jiménez, J., Moin, P., 1991. The minimal flow unit in near-wall turbulence. J. Fluid Mech. 225, 213–240.

Kachanov, Y.S., Kozlov, V.V., Levchenko, V.Y., Ramazov, M.P., 1985. On the nature of K-breakdown of a laminar boundary layer. In: Kozlov, V.V. (Ed.), Laminar–Turbulent Transition. Springer, New York, pp. 61–73.

Kirby, M., Armbruster, D., 1992. Reconstructing phase space from PDE simulations. Z. Angew. Math. Phys. 43, 999–1022.

Kline, S.J., Reynolds, W.C., Schraub, F.A., Runstadler, P.W., 1967. The structure of turbulent boundary layers. J. Fluid Mech. 30, 741–773.

Lumley, J.L., 1967. The structure of inhomogeneous turbulence. In: Yaglom, A.M., Tatarski, V.I. (Eds.), Atmospheric Turbulence and Wave Propagation. Nauka, Moscow, pp. 166–178.

Lumley, J.L. (Ed.), 1990. Whither Turbulence? Turbulence at the Crossroads. Lecture Notes in Physics, vol. 357. Springer, Berlin.

Moin, P., 1984. Probing turbulence via large eddy simulation. AIAA paper 84-0174.

Moin, P., Moser, R.D., 1989. Characteristic-eddy decomposition of turbulence in a channel. J. Fluid Mech. 200, 471–509.

Noack, B.R., Eckelmann, H., 1992. On chaos in wakes. Physica D 56, 151–164.

Noack, B.R., Eckelmann, H., 1994a. A low dimensional Galerkin method for the three-dimensional flow around a circular cylinder. Phys. Fluids 6, 124–143.

Noack, B.R., Eckelmann, H., 1994b. Theoretical investigation of the bifurcations and the turbulence attractor of the cylinder wake. Z. Angew. Math. Mech. 74, T396–T397.

Noack, B.R., Eckelmann, H., 1994c. A global stability analysis of the steady and periodic cylinder wake. J. Fluid Mech. 270, 297–330.

Ott, E., Grebogi, C., Yorke, J.A., 1990. Controlling chaos. Phys. Rev. Lett. 64, 1196–1199.

Park, H., Sirovich, L., 1990. Turbulent thermal convection in a finite domain, Part II. Numerical results. Phys. Fluids A 2 (9), 1659–1668.

Podvin, B., Gibson, J., Berkooz, G., Lumley, J., 1997. Lagrangian and Eulerian view of the bursting period. Phys. Fluids 9 (2), 433–437.

Rajaee, M., Karlsson, S.K.F., 1990. Shear flow coherent structures via Karhunen–Loève expansion. Phys. Fluids A 2, 2249–2251.

Rajaee, M., Karlsson, S.K.F., 1992. On the Fourier space decomposition of free shear flow measurements and mode degeneration in the pairing process. Phys. Fluids A 4, 321–339.

Rajaee, M., Karlsson, S.K.F., Sirovich, L., 1994. Low-dimensional description of free-shear-flow coherent structures and their dynamical behaviour. J. Fluid Mech. 258, 1–29.

Rempfer, D., 1993. Low dimensional models of a flat-plate boundary layer. In: So, R.M.C., Speciale, C.G., Launder, B.E. (Eds.), Near-Wall Turbulent Flows. Elsevier, Amsterdam. pp. 63–72.

Rempfer, D., 1994. On the structure of dynamical systems describing the evolution of coherent structures in a convective boundary layer. Phys. Fluids 6 (3), 1402–1404.

Rempfer, D., Fasel, H., 1991. Evolution of coherent structures during transition in a flat-plate boundary layer. In: Proc. 8th Symp. on Turbulent Shear Flows 1, 18.3.1–18.3.6.

Rempfer, D., Fasel, H., 1993. The dynamics of coherent structures in a flat-plate boundary layer. Appl. Sci. Res. 51, 73–77.

Rempfer, D., Fasel, H., 1994a. Evolution of three-dimensional coherent structures in a flat-plate boundary layer. J. Fluid Mech. 260, 351–375.

Rempfer, D., Fasel, H., 1994b. Dynamics of three-dimensional coherent structures in a flat-plate boundary layer. J. Fluid Mech. 275, 257–283.

Rist, U., Fasel, H., 1995. Direct numerical simulation of controlled transition in a flat-plate boundary layer. J. Fluid Mech. 298, 211–248.

Robinson, S.K., 1991. Coherent motions in the turbulent boundary layer. Ann. Rev. Fluid Mech. 23, 601–639.

Rodriguez, J.D., Sirovich, L., 1990. Low-dimensional dynamics for the complex Ginzburg–Landau equation. Physica D 43, 77–86.

Ruelle, D., Takens, F., 1970. On the nature of turbulence. Comm. Math Phys. 20, 167–192.

Sanghi, S., Aubry, N., 1993. Mode interaction models for near-wall turbulence. J. Fluid Mech. 247, 455–488.

Sirovich, L., 1987. Turbulence and the dynamics of coherent structures. I. Coherent structures. II. Symmetries and transformations. III. Dynamics and scaling. Quart. Appl. Math. 45, 561–590.

Sirovich, L., 1989. Chaotic dynamics of coherent structures. Physica D 37, 126–143.

Sirovich, L., Deane, A.E., 1991. A computational study of Rayleigh–Bénard convection. Part II. Dimension considerations. J. Fluid Mech. 222, 251–265.

Sirovich, L., Maxey, M., Tarman, H., 1989. An eigenfunction analysis of turbulent thermal convection. In: André, J.-C., Coustieux, J., Durst, F., Launder, B.E., Schmidt, F.W., Whitelaw, J.H. (Eds.), Turbulent Shear Flows 6. Springer, New York, pp. 68–77.

Sirovich, L., Park, H., 1990. Turbulent thermal convection in a finite domain, Part I. Theory. Phys. Fluids A 2 (9), 1649–1658.

Sirovich, L., Rodriguez, J.D., 1987. Coherent structures and chaos: a model problem. Phys. Lett. A 120 (5), 211–214.

Sivashinsky, G.I., 1977. Nonlinear analysis of hydrodynamic instability in laminar flames, Part I: derivation of the basic equations. Acta Astronaut. 4, 1176–1206.

Stone, E., Holmes, P., 1989. Noise induced intermittency in a model of a turbulent boundary layer. Physica D 37, 20–32.

Stone, E., Holmes, P., 1990. Random perturbations of heteroclinic cycles. SIAM J. Appl. Math. 50, 726–743.

Temam, R., 1988. Infinite-Dimensional Dynamical Systems in Mechanics and Physics. Springer, New York.

Tennekes, H., Lumley, J.L., 1972. A First Course in Turbulence. The MIT Press, Cambridge, MA.

Zheng, X., Glauser, M.N., 1990. A low dimensional description of the axisymmetric jet mixing layer. ASME Comput. Eng. 2, 121–127.

Zhou, X., Sirovich, L., 1992. Coherence and chaos in a model of turbulent boundary layer. Phys. Fluids A 4, 2855–2874.